bioRxiv preprint doi: https://doi.org/10.1101/2021.08.15.456427; this version posted August 16, 2021. The copyright holder for this preprint (which was not certified by peer review) is the author/funder, who has granted bioRxiv a license to display the preprint in perpetuity. It is made available under aCC-BY-NC-ND 4.0 International license.

Title:

Nos2$^{-/-}$ mice infected with *M. tuberculosis* develop neurobehavioral changes and immunopathology mimicking human central nervous system tuberculosis

Authors:

Xuan Ying Poh[1], Jia Mei Hong[1], Chen Bai[1], Qing Hao Miow[1], Pei Min Thong[1], Yu Wang[1], Ravisankar Rajarethinam[2], Catherine W.M. Ong[1, 3, 4*]

Affiliations:

[1]Infectious Diseases Translational Research Programme, Department of Medicine, Yong Loo Lin School of Medicine, National University of Singapore, Singapore

[2]Advanced Molecular Pathology Laboratory, Institute of Molecular and Cell Biology, Agency for Science, Technology and Research (A*STAR), Singapore

[3] Division of Infectious Diseases, Department of Medicine, National University Hospital

[4] Institute for Health Innovation and Technology (iHealthtech), National University of Singapore

*** Corresponding author**

Catherine W.M. Ong

bioRxiv preprint doi: https://doi.org/10.1101/2021.08.15.456427; this version posted August 16, 2021. The copyright holder for this preprint (which was not certified by peer review) is the author/funder, who has granted bioRxiv a license to display the preprint in perpetuity. It is made available under aCC-BY-NC-ND 4.0 International license.

10th floor, Tower Block,

1E Kent Ridge Road

Singapore 119228

Email: Catherine_wm_ong@nuhs.edu.sg

Abstract word count (limit): 145 (150)

Word count: 3896

Page numbers: 43

Figures: 6

Tables: 2

Video 1. Saline control *Nos2*$^{-/-}$ mice

Video 2. *Nos2*$^{-/-}$ mice infected with *M.tb* via the i.c.vent. route exhibited myoclonic jerks and limb weakness.

Supplementary Tables: 1

Supplementary Figures: 7

bioRxiv preprint doi: https://doi.org/10.1101/2021.08.15.456427; this version posted August 16, 2021. The copyright holder for this preprint (which was not certified by peer review) is the author/funder, who has granted bioRxiv a license to display the preprint in perpetuity. It is made available under aCC-BY-NC-ND 4.0 International license.

ABSTRACT (150 words max)

Understanding the pathophysiology of central nervous system tuberculosis (CNS-TB) is hampered by the lack of a good pre-clinical model that mirrors the human CNS-TB infection. We developed a murine CNS-TB model that demonstrates neurobehavioral changes with similar immunopathology with human CNS-TB. Intra-cerebroventricular (i.c.vent.) infection of *Nos2*$^{-/-}$ mice with *Mycobacterium tuberculosis* (*M.tb*) led to development of neurological signs and more severe brain granulomas compared to C3HeB/FeJ mice. Compared with CDC1551 *M.tb*, H37Rv *M.tb* infection resulted in a higher neurobehavioral score and earlier mortality. I.c.vent. infection caused necrotic neutrophil-dominated pyogranulomas in the brain relative to intravenous (i.v.) infection which resulted in disseminated granulomas and mycobacteraemia. Immunological analysis found H37Rv i.c.vent.-infected mice to demonstrate higher brain concentrations of inflammatory cytokines, chemokines and adhesion molecule ICAM-1 than H37Rv i.v.-infected mice. Our murine CNS-TB model serves as a pre-clinical platform to dissect host-pathogen interactions and evaluate therapeutic agents for CNS-TB.

bioRxiv preprint doi: https://doi.org/10.1101/2021.08.15.456427; this version posted August 16, 2021. The copyright holder for this preprint (which was not certified by peer review) is the author/funder, who has granted bioRxiv a license to display the preprint in perpetuity. It is made available under aCC-BY-NC-ND 4.0 International license.

INTRODUCTION

The most severe form of *Mycobacterium tuberculosis* (*M.tb*) infection is central nervous system tuberculosis (CNS-TB) which has high mortality and serious long-term neurological sequelae even with effective anti-tuberculous treatment (Rock, Olin, Baker, Molitor, & Peterson, 2008; The Lancet, 2011; Wilkinson et al., 2017). Common manifestations of human CNS-TB are tuberculous meningitis (TBM), tuberculomas and tuberculous brain abscesses (Rom, 2004). Cerebral vasculitis and inflammation resulting in infarcts is the primary cause of permanent brain tissue damage in TBM and is among the worst consequences of CNS-TB (P. R. Donald & Schoeman, 2004; Lammie, Hewlett, Schoeman, & Donald, 2009). Despite effective TB treatment with antibiotics and adjunctive corticosteroids, CNS-TB remains one of the more challenging clinical syndromes to manage.

To advance our understanding of CNS-TB, we need an appropriate animal model that recapitulates the neurobehavioral, immunopathological and histopathological changes in human CNS-TB to dissect pathogenesis and aid drug discovery. Several animal models of CNS-TB have been described, including guinea pigs, rabbits, mice, pigs, and zebrafish. The rabbit model closely mimics human disease, developing clinical and histological changes (Bolin et al., 1997; Mazzolla et al., 2002; Shope & Lewis, 1929; Swaim et al., 2006; Tsenova et al., 2002; Tsenova, Sokol, Freedman, & Kaplan, 1998; Tucker et al., 2016). However, a number of immunological tools profiling protein secretion and gene expression are unavailable for rabbits (Rock et al., 2008) and therefore preclude their suitability for in-depth immunological studies.

bioRxiv preprint doi: https://doi.org/10.1101/2021.08.15.456427; this version posted August 16, 2021. The copyright holder for this preprint (which was not certified by peer review) is the author/funder, who has granted bioRxiv a license to display the preprint in perpetuity. It is made available under aCC-BY-NC-ND 4.0 International license.

The mouse model has many advantages over other animals, including the availability of genetic and molecular tools as well as cost-effectiveness for large studies. However, existing murine CNS-TB models do not display the clinical features and immunological phenotypes of CNS-TB observed in humans. C57BL/6 mice are generally resistant to CNS-TB infection, with no pathological abnormalities detected and no observed mortality over 24 weeks of study (van Well et al., 2007). BALB/c mice infected through the intracerebral route directly into the brain parenchyma with *Mycobacterium bovis* BCG (BCG) had infiltration of inflammatory cells, but no granulomas were observed (Mazzolla et al., 2002). This contrasts with human CNS-TB where tuberculomas occur in approximately 30% of TBM patients (Schaller, Wicke, Foerch, & Weidauer, 2019). Intravenous inoculation of BALB/c mice with *M.tb* strain CDC1551 successfully infected the CNS but did not produce granulomas in the brain and had low expression of brain chemokines and cytokines IL-1β, IL-6, TNF-α and IFN-γ, in contrast to the increased expression of these cytokines in the cerebrospinal fluid (CSF) of human TBM patients (Be et al., 2008; Sharma et al., 2017). While some murine CNS-TB models have meningitis and/or brain granulomas, they do not demonstrate neurological signs of disease and mortality, unlike human CNS-TB (van Well et al., 2007; Zucchi et al., 2012). Given the varying susceptibility and pathology of CNS-TB infection in different mouse strains, genetic predisposition is likely to play a crucial role. C3HeB/FeJ "Kramnik" mice were found to be hyper susceptible to *M.tb* infection due to the presence of an allele, termed the "super susceptibility to tuberculosis 1" (*sst1*) locus, and developed a more human-like lung pathology in contrast to C57BL/6 mice (Irwin et al., 2015; Kramnik, Dietrich, Demant, & Bloom, 2000). However, the ability of C3HeB/FeJ mice to develop CNS-TB remains to be explored.

Intracerebral-infection with *M.tb* H37Rv directly into the brain parenchyma of inducible nitric oxide synthase (iNOS)-knockout mice resulted in neurological signs with meningitis, and mice

bioRxiv preprint doi: https://doi.org/10.1101/2021.08.15.456427; this version posted August 16, 2021. The copyright holder for this preprint (which was not certified by peer review) is the author/funder, who has granted bioRxiv a license to display the preprint in perpetuity. It is made available under aCC-BY-NC-ND 4.0 International license.

exhibited 63% mortality post-infection (p.i.) (Olin et al., 2008). However, the development of intracerebral tuberculomas and immunological profile were not phenotyped in this mouse model. Cytokine-induced upregulation of iNOS or NOS2 by murine macrophages have been implicated in the killing of intracellular pathogens such as *M.tb*, but the role of this antimicrobial system in human macrophages remains unclear (Chan, Chan, & Schluger, 2001; Schneemann & Schoeden, 2007). Studies have shown that activated human microglia, the brain resident macrophages, do not express iNOS (Lee, Dickson, Liu, & Brosnan, 1993; Rock et al., 2005) or reactive nitrogen intermediate (RNI) nitric oxide (NO) (Peterson, Hu, Anderson, & Chao, 1994), whereas murine microglia produced substantial amounts of NO on activation (Peterson et al., 1994). Given the well-established role of macrophages in TB, the inter-species difference in microglia expression of iNOS may explain the species tropism barrier to the development of CNS-TB in mice.

To address the limitations of existing murine CNS-TB models, we explored the effects of mouse strains, *M.tb* strains and routes of infection on the development of CNS-TB disease. First, we compared two mouse strains, C3HeB/FeJ and *Nos2*$^{-/-}$ mice, to investigate whether the *sst1* locus or *Nos2* gene plays a more important role in CNS-TB infection. After selecting the suitable mouse strain, we investigated the effects of two different *M.tb* strains, H37Rv and CDC1551, and two routes of infection: intra-cerebroventricular (i.c.vent.) into the third ventricle and intravenous (i.v.), on the development of a murine CNS-TB model with human-like pathology. The i.c.vent. route of infection mimics the rupture of meningeal tuberculous lesions and the subsequent release of *M.tb* into the CSF, whereas the i.v. route mimics the hematogenous spread of *M.tb.* In this study, we showed that i.c.vent. infection of *Nos2*$^{-/-}$ mice with *M.tb* H37Rv developed the most severe neurological symptoms and induced a high expression of adhesion molecules, chemokines, and inflammatory cytokines in the brain,

bioRxiv preprint doi: https://doi.org/10.1101/2021.08.15.456427; this version posted August 16, 2021. The copyright holder for this preprint (which was not certified by peer review) is the author/funder, who has granted bioRxiv a license to display the preprint in perpetuity. It is made available under aCC-BY-NC-ND 4.0 International license.

consistent with the infiltration of inflammatory cells and pathological changes. This pre-clinical model can be used to understand the mechanisms in host immunopathology and evaluate treatment for CNS-TB.

bioRxiv preprint doi: https://doi.org/10.1101/2021.08.15.456427; this version posted August 16, 2021. The copyright holder for this preprint (which was not certified by peer review) is the author/funder, who has granted bioRxiv a license to display the preprint in perpetuity. It is made available under aCC-BY-NC-ND 4.0 International license.

RESULTS

M.tb infected *Nos2*$^{-/-}$ strain exhibited worse neurobehavioral score and worse histopathological changes in the brain than C3HeB/FeJ strain

To investigate whether *Nos2*$^{-/-}$ or C3HeB/FeJ mice better replicate human CNS-TB , we inoculated each mouse with $9.15 \pm 2.33 \times 10^4$ colony forming units (CFU; mean ± s.d) of *M.tb* CDC1551 into the third ventricle to infect the meninges (Supplementary figure 1). Infected *Nos2*$^{-/-}$ mice displayed neurological symptoms such as twitching and limb weakness from 3 weeks post-infection (p.i.) (Video 2) that were not observed in infected C3HeB/FeJ mice or saline control mice (Video 1). Infected *Nos2*$^{-/-}$ mice had significantly higher neurobehavioral scores than infected C3HeB/FeJ mice at 4 and 8 weeks p.i. (Figure 1a, $p < 0.0001$ and $p < 0.0001$ respectively). Neurological behavior assessed include tremors, twitches and appearance of eyes, with higher neurobehavioral scores reflecting an increasing severity of neurological deficits. CFU enumeration showed that brain and lung homogenates of infected *Nos2*$^{-/-}$ mice had higher mycobacterial load compared to infected C3HeB/FeJ mice that had a trend to statistical significance (Figure 1b). Median (IQR) brain CFU count in *Nos2*$^{-/-}$ and C3HeB/FeJ mice was 5×10^5 ($1.65 \times 10^5 – 5.8 \times 10^5$) compared to 9.75×10^2 ($6.25 \times 10^1 – 5 \times 10^3$) respectively ($p = 0.057$), while median (IQR) lung CFU count was 1.00×10^3 ($6.5 \times 10^2 – 1.5 \times 10^3$) in infected *Nos2*$^{-/-}$ mice and 0 (0 – 75) in infected C3HeB/FeJ mice ($p = 0.057$). Mycobacterial load in the liver, spleen and blood were similar.

bioRxiv preprint doi: https://doi.org/10.1101/2021.08.15.456427; this version posted August 16, 2021. The copyright holder for this preprint (which was not certified by peer review) is the author/funder, who has granted bioRxiv a license to display the preprint in perpetuity. It is made available under aCC-BY-NC-ND 4.0 International license.

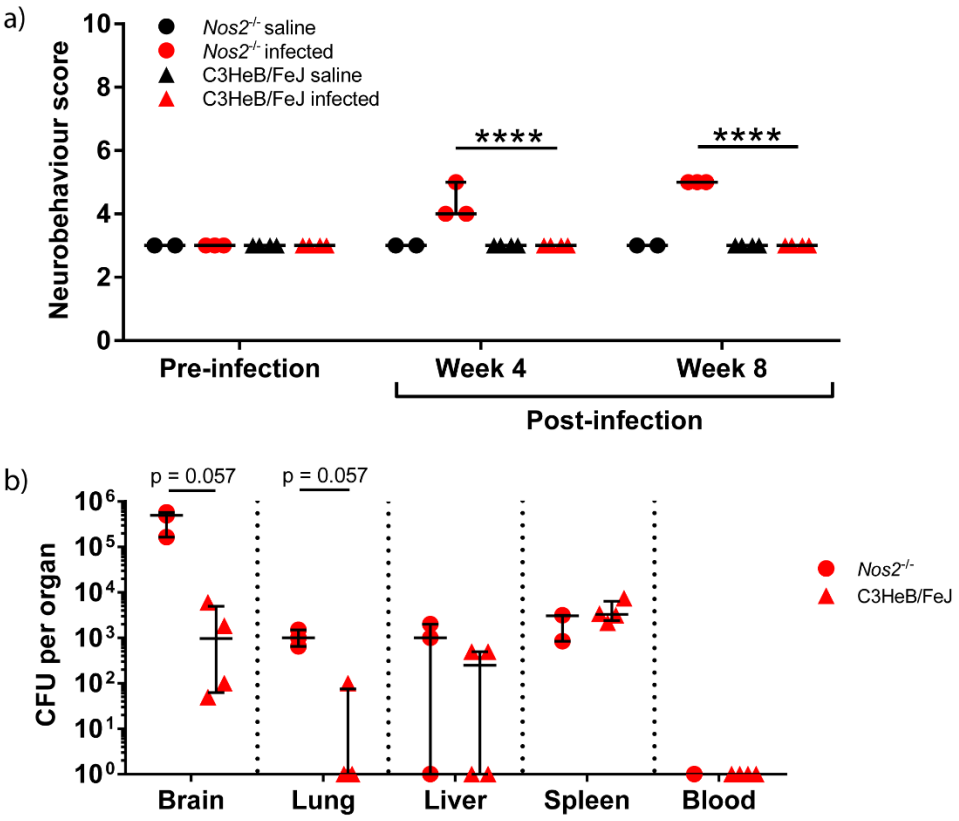

Figure 1. *Nos2*$^{-/-}$ strain exhibited higher neurobehavioral score and increased *M.tb* CFU in the brain compared to C3HeB/FeJ strain post-i.c.vent. infection. (a) Neurobehavioral scores were significantly higher in infected *Nos2*$^{-/-}$ mice at 4 and 8 weeks p.i. compared with infected C3HeB/FeJ mice. Parameters assessed include tremors, twitches and appearance of eyes, with higher neurobehavioral scores reflecting an increasing severity of neurological deficits. ****, $p < 0.0001$. (b) *M.tb* colony forming units (CFU) in the brain and lung of *Nos2*$^{-/-}$ is higher compared to C3HeB/FeJ mice. At day 56 p.i., brain, lung, liver, spleen and blood were processed for enumeration of mycobacterial load.

Although there were no macroscopic changes in the brain, lung and spleen between the two mouse strains (Figure 2a), histopathological analysis revealed considerable differences between these two strains (Figure 2b). Infected *Nos2*$^{-/-}$ mice demonstrated more inflammatory

bioRxiv preprint doi: https://doi.org/10.1101/2021.08.15.456427; this version posted August 16, 2021. The copyright holder for this preprint (which was not certified by peer review) is the author/funder, who has granted bioRxiv a license to display the preprint in perpetuity. It is made available under aCC-BY-NC-ND 4.0 International license.

cell infiltrate in the brain parenchyma compared to infected C3HeB/FeJ mice. We postulated that the increase in leukocyte inflammation might be due to increased expression of adhesion molecules in the brain, and confirmed a significantly higher concentration of ICAM-1 and p-selectin in infected *Nos2*$^{-/-}$ than C3HeB/FeJ mice (Figure 2c and d). Brain concentration of ICAM-1 and p-selectin were 14-fold ($p = 0.0089$) and 10-fold ($p = 0.0008$) higher in infected *Nos2*$^{-/-}$ compared to C3HeB/FeJ mice.

Next, we investigated further the mechanism behind the increased immune cell recruitment in infected *Nos2*$^{-/-}$ mice. As TB is characterised by a Th1 inflammatory response, we examined the concentrations of Th1 cytokines and chemokines. Concentrations of neutrophil chemoattractants were also profiled as histopathological analysis showed marked neutrophilic inflammation. Concentrations of Th1-associated inflammatory mediators TNF-α and CXCL-10 were significantly higher in infected *Nos2*$^{-/-}$ mice than infected C3HeB/FeJ mice, while IFN-γ and CCL-5 showed a trend to increase (Figure 3a, b, c and d). Infected *Nos2*$^{-/-}$ mice also had a significantly higher concentration of chemoattractants, CXCL-1, CXCL-2 and LIX, than infected C3HeB/FeJ mice (Figure 3e, f and g), which may explain the neutrophilic infiltration in the brain and meninges of *Nos2*$^{-/-}$ *M.tb*-infected mice relative to the C3HeB/FeJ *M.tb*-infected mice. As *Nos2*$^{-/-}$ mice displayed a greater severity of CNS-TB disease than C3HeB/FeJ mice in terms of neurobehavior, histopathology, and immunological profile, the *Nos2*$^{-/-}$ mouse strain was chosen for all subsequent experiments.

bioRxiv preprint doi: https://doi.org/10.1101/2021.08.15.456427; this version posted August 16, 2021. The copyright holder for this preprint (which was not certified by peer review) is the author/funder, who has granted bioRxiv a license to display the preprint in perpetuity. It is made available under aCC-BY-NC-ND 4.0 International license.

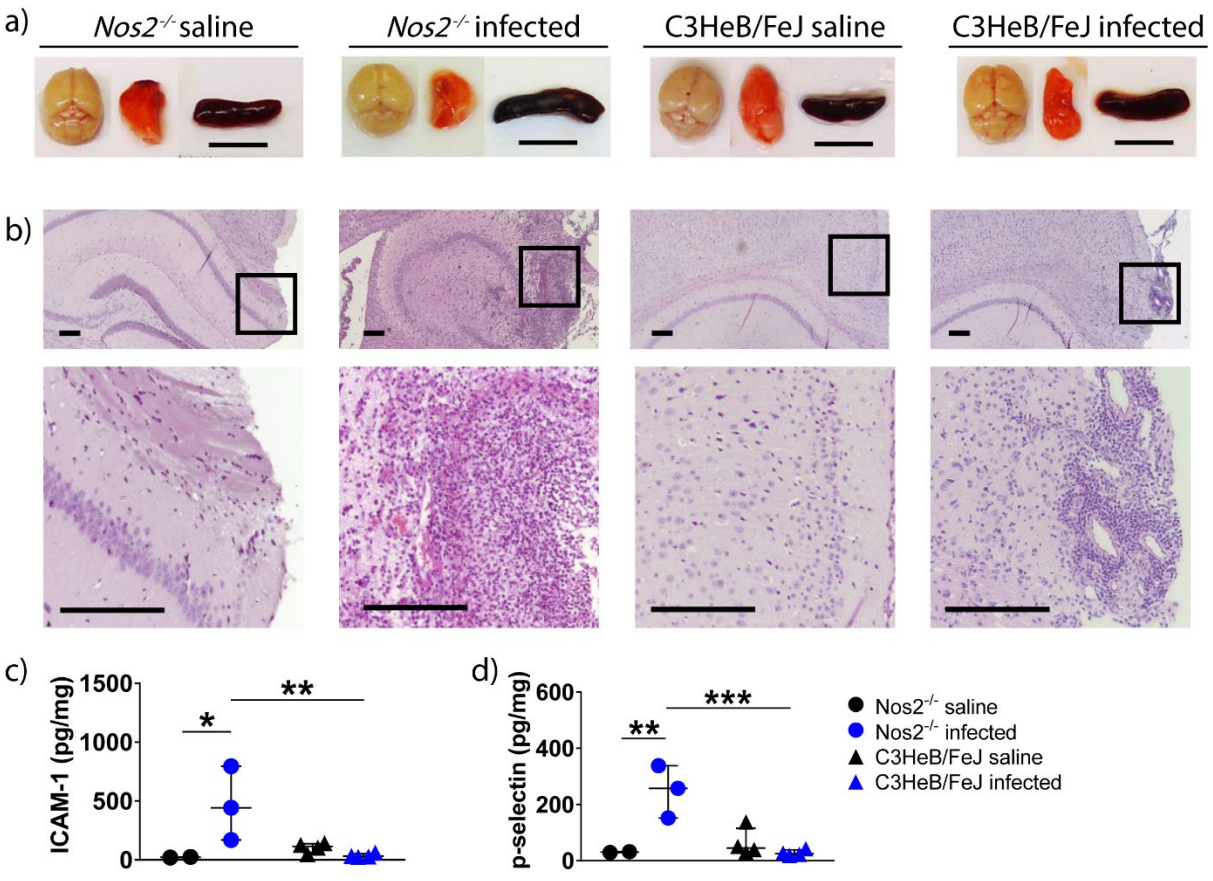

Figure 2. *Nos2*$^{-/-}$ strain demonstrates more inflammatory cell infiltrate in the brain and meninges with increased concentrations of adhesion molecules compared to C3HeB/FeJ strain at 8 weeks p.i. (a) Macroscopic assessment of brain, lung and spleen of *M.tb* infected Nos2$^{-/-}$ and C3HeB/FeJ mice were similar to saline controls. Images are representative of 2-4 mice per condition. Scale bar = 1 cm. (b) Hematoxylin and eosin (H&E) stain of a representative brain section from each group is shown, demonstrating normal brain histology in saline control mice and histopathology in infected mice. High-power views (insets) demonstrate more inflammatory cell infiltrate in the brain of infected *Nos2*$^{-/-}$ compared to C3HeB/FeJ mice. Scale bar = 200 µm. (c and d) Infected *Nos2*$^{-/-}$ have increased concentrations of (c) ICAM-1 and (d) p-selectin in the brain compared to C3HeB/FeJ mice. Adhesion molecule concentrations were normalised to total protein concentration and compared using two-way ANOVA with Sidak's multiple comparisons test. Bars represent median and IQR. *, $p < 0.05$; **, $p < 0.01$; ***, $p < 0.001$.

bioRxiv preprint doi: https://doi.org/10.1101/2021.08.15.456427; this version posted August 16, 2021. The copyright holder for this preprint (which was not certified by peer review) is the author/funder, who has granted bioRxiv a license to display the preprint in perpetuity. It is made available under aCC-BY-NC-ND 4.0 International license.

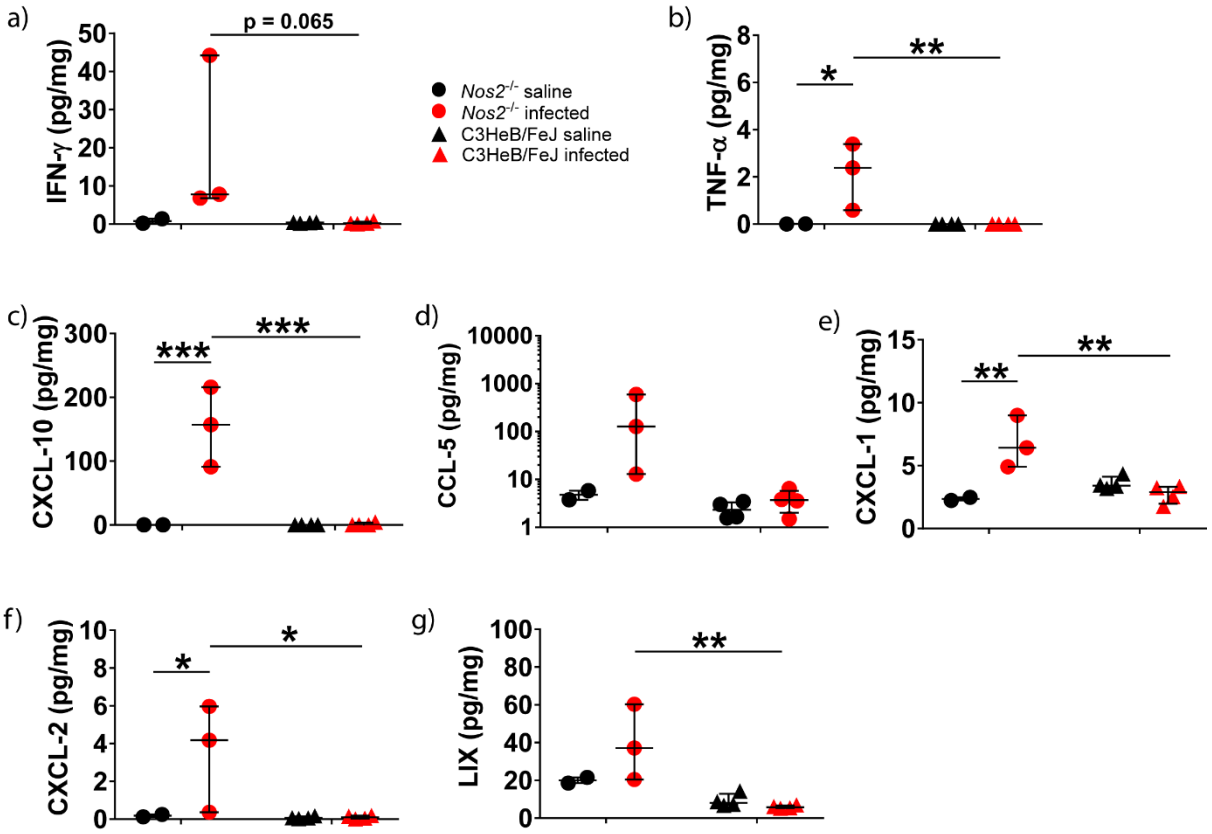

194

195 **Figure 3. I.c.vent.-infected *Nos2*$^{-/-}$ mice demonstrated increased concentration of Th1-associated**
196 **cytokines and chemokines, and neutrophil chemoattractants compared to C3HeB/FeJ infected**
197 **mice at 8 weeks p.i..** Concentrations of chemokines and cytokines in brain homogenates were
198 normalised against total protein concentration. Statistical analysis performed using two way ANOVA
199 with Sidak's multiple comparisons test. Bars represent median and IQR. *, $p < 0.05$; **, $p < 0.01$; ***,
200 $p < 0.001$.

201

bioRxiv preprint doi: https://doi.org/10.1101/2021.08.15.456427; this version posted August 16, 2021. The copyright holder for this preprint (which was not certified by peer review) is the author/funder, who has granted bioRxiv a license to display the preprint in perpetuity. It is made available under aCC-BY-NC-ND 4.0 International license.

I.c.vent. infection by H37Rv *M.tb* strain resulted in a worse neurobehavioral score, earlier mortality and increased mycobacterial load in the brain than CDC1551 *M.tb* strain

We further compared two different *M.tb* strains, H37Rv and CDC1551, on the neurobehavioral scores and mortality outcomes. At day 28 p.i., infected mice had a significantly lower weight than saline control, independent of the routes of infection (Figure 4a and Supplementary figure 2a). Within the i.c.vent. group, weight change between H37Rv- and CDC1551-infected mice were similar throughout the study (Figure 4a). However, within the i.v. group, the weight change in H37Rv-infected mice at day 28 p.i. was -3.6 $\pm$ 3.1% (mean $\pm$ s.d.) which was significantly different from CDC1551-infected mice that gained a mean weight of 6.0 $\pm$ 2.4% ($p = 0.0027$) (Supplementary figure 2a).

By day 28 p.i., 3 out of 6 (50%) H37Rv i.c.vent.-infected mice were euthanized as they reached the humane end point, compared to 1 out of 5 (20%) in CDC1551-infected mice (Figure 4b). As infection progressed, neurological signs in surviving H37Rv i.c.vent. mice worsened with a higher neurobehavioral score than CDC1551 i.c.vent. mice by week 8 p.i.. Median (IQR) neurobehavioral score in H37Rv i.c.vent. mice was 5.5 (5-6) as compared to 4 (4-4) in CDC1551 i.c.vent. infected mice ($p < 0.0001$) (Figure 4c).

Within the group of i.v.-infected mice, H37Rv *M.tb* also resulted in higher mortality than CDC1551. *M.tb* H37Rv-infected mice displayed uniform lethality by day 30 p.i., while 100% survival was observed in CDC1551-infected mice (Supplementary figure 2b). The findings from the survival curve are also reflected in the neurobehavioral score over time, as CDC1551 i.v. mice displayed mild to no neurological signs at week 8 p.i. (Supplementary figure 2c).

bioRxiv preprint doi: https://doi.org/10.1101/2021.08.15.456427; this version posted August 16, 2021. The copyright holder for this preprint (which was not certified by peer review) is the author/funder, who has granted bioRxiv a license to display the preprint in perpetuity. It is made available under aCC-BY-NC-ND 4.0 International license.

On gross pathology examination, we found that both H37Rv and CDC1551 i.v.-infected mice (Supplementary figure 2d) and H37Rv i.c.vent.-infected mice had enlarged spleen relative to saline controls (Figure 4d), indicating dissemination of infection. CDC1551 i.v.-infected mice developed macroscopic granulomas in the lungs (Supplementary figure 2d) that was not observed in other groups. I.v. inoculation of *M.tb*, independent of *M.tb* strains, resulted in a disseminated infection with granuloma formation in the heart, kidneys, and spleen, which was not observed in i.c.vent.-infected mice (Supplementary figure 2e). Intra-abdominal abscesses were also found in one of the H37Rv i.v.-infected mice examined (data not shown). This was consistent with the blood culture results, where mycobacteraemia was detected in six out of 12 (50%) mice infected by the i.v. route (Supplementary figure 2f). There was no mycobacteremia in any of the i.c.vent.-infected mice (n = 11) (Figure 4e). H37Rv i.c.vent.-infected mice demonstrated a trend towards increased *M.tb* load in the brain than CDC1551 i.c.vent., with median brain CFU count of 4.3×10^6 in H37Rv i.c.vent. and 4.9×10^5 in CDC1551 i.c.vent. mice ($p = 0.052$). Interestingly, although no mycobacteremia was found in i.c.vent.-infected mice, *M.tb* was cultured from the lungs with comparable mycobacterial load in both *M.tb* strains. Median lung CFU count was 2.9×10^4 and 5.0×10^2 in H37Rv and CDC1551 i.c.vent. mice respectively ($p = 0.33$) (Figure 4e). The presence of *M.tb* in the brain was confirmed by Ziehl-Neelsen staining, with numerous intra- and extra-cellular bacilli within the brain granulomatous lesion (Figure 4f).

Collectively, these results showed that H37Rv *M.tb* is more suited than CDC1551 *M.tb* for the murine CNS-TB model as H37Rv infection resulted in earlier mortality, worse neurobehavioral score and increased mycobacterial load in the brain compared to CDC1551 infection. I.c.vent infection also resulted in a more localized infection relative to the widespread dissemination observed in the i.v-infected mice.

bioRxiv preprint doi: https://doi.org/10.1101/2021.08.15.456427; this version posted August 16, 2021. The copyright holder for this preprint (which was not certified by peer review) is the author/funder, who has granted bioRxiv a license to display the preprint in perpetuity. It is made available under aCC-BY-NC-ND 4.0 International license.

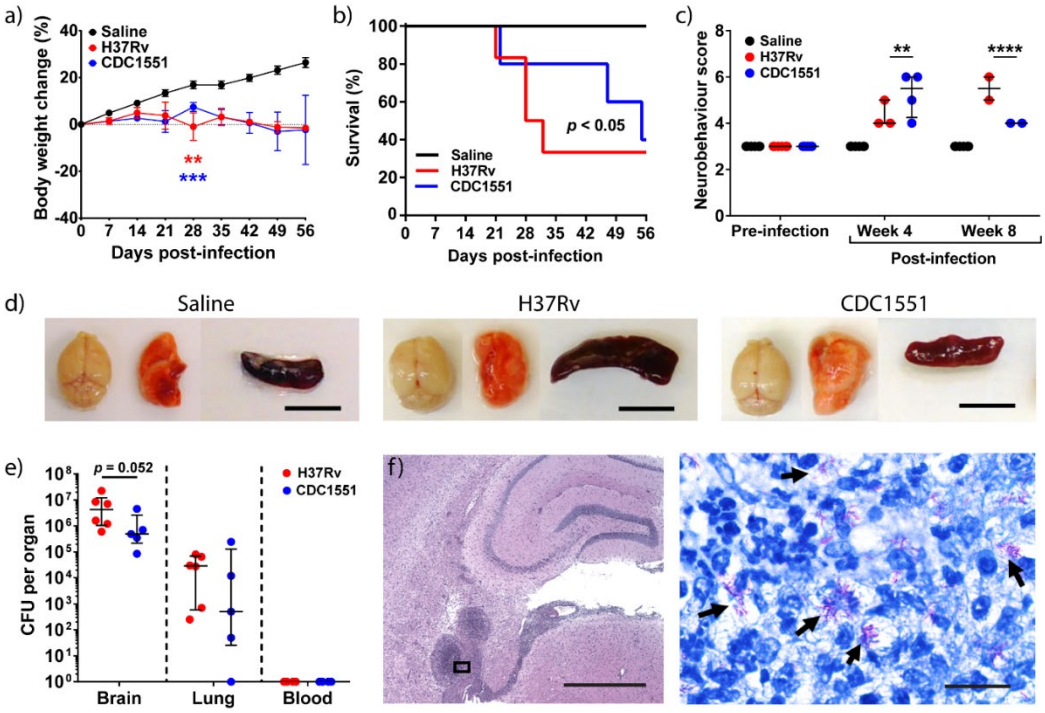

Figure 4. I.c.vent. infection with H37Rv resulted in earlier mortality, higher neurobehavioral score, and increased mycobacterial load in the brain compared to CDC1551. (a) *M.tb*-infected mice lost significantly more weight than saline control. Percentage change in body weight relative to initial body weight at day 0 p.i. is shown. Bars represent mean ± SEM. **, $p < 0.01$; ***, $p < 0.001$. Statistical analysis between H37Rv-infected mice and saline controls in red asterisks, while comparisons between CDC1551-infected mice and saline controls in blue asterisks. (b) Kaplan-Meier curve shows a significant difference in survival between the groups. (c) H37Rv i.c.vent. demonstrate higher neurobehavioral score at 8 weeks p.i. compared to CDC1551 i.c.vent. mice. **, $p < 0.01$; ****, $p < 0.0001$. (d) Gross pathological examination of brain, lung and spleen show no difference between saline control and *M.tb*-infected mice except for enlarged spleen in H37Rv i.c.vent-infected mice. Scale bar = 1 cm. (e) H37Rv-infected mice show a trend towards increased *M.tb* load in the brain, while lung and blood CFU were comparable to CDC1551-infected mice. Bars represent median and IQR. (f) Low-power view of a representative H&E-stained granuloma in the brain of H37Rv i.c.vent. mice. High-power view (inset) demonstrates numerous intra- and extracellular acid-fast bacilli (black arrows) by Ziehl-Neelson (ZN) stain within the brain granuloma. Scale bars represent 1 mm in H&E stain and 20 µm in ZN stain. 5-6 mice were used per experimental condition.

bioRxiv preprint doi: https://doi.org/10.1101/2021.08.15.456427; this version posted August 16, 2021. The copyright holder for this preprint (which was not certified by peer review) is the author/funder, who has granted bioRxiv a license to display the preprint in perpetuity. It is made available under aCC-BY-NC-ND 4.0 International license.

H37Rv infection via the i.c.vent. route resulted in pyogranuloma formation with increased expression of adhesion molecules relative to the i.v. route.

We next conducted a thorough histological evaluation in *Nos2*$^{-/-}$ mice infected with H37Rv via either the i.v. or i.c.vent. route. Histopathological evaluation demonstrated that i.c.vent.-infected *Nos2*$^{-/-}$ mice developed more severe meningitis and parenchymal granulomas compared to i.v.-infected mice, independent of *M.tb* strains (Figure 5a-c and Supplementary figure 3). In the brain, *M.tb*-induced pathological lesions included mononuclear cell (MNC) inflammation, gliosis, neuronal degeneration, granuloma, pyogranuloma, liquefactive necrosis, and perivascular cuffing (Supplementary figure 4). Consistent with the more pronounced brain inflammation, H37Rv i.c.vent.-infected mice had a higher histopathological score than H37Rv i.v. mice (Table 1). In addition, the meningitis and parenchymal inflammation in the brain of H37Rv i.c.vent.-infected mice were extensive, extending far beyond the injection site with a total spread of 2500 µm in the anterior-posterior axis (Supplementary figure 5). While all infected mice developed brain granulomas independent of the routes of infection and *M.tb* strain, pyogranulomas were only present in i.c.vent.-infected mice. These pyogranulomatous lesions contained a central area of liquefactive necrosis with abundant degenerated polymorphs surrounded with MNCs such as macrophages, which were sometimes epithelioid, and lymphocytes enclosed within a thin layer of fibrous capsule (Figure 5d). These necrotic brain lesions are a key feature in human CNS-TB patients (Zaharie et al., 2020). In addition, the presence of neutrophils in CNS tuberculous granulomas was also demonstrated in human brain biopsies with histologically proven CNS-TB (Ong et al., 2017). Collectively, these results demonstrate that i.c.vent. infection of *Nos2*$^{-/-}$ mice with H37Rv produces a murine CNS-TB model that resembles human necrotic TB granulomas, and also recapitulates the cellular architecture of human CNS-TB tuberculomas.

bioRxiv preprint doi: https://doi.org/10.1101/2021.08.15.456427; this version posted August 16, 2021. The copyright holder for this preprint (which was not certified by peer review) is the author/funder, who has granted bioRxiv a license to display the preprint in perpetuity. It is made available under aCC-BY-NC-ND 4.0 International license.

To analyse the extent of granulomatous inflammation, we measured the number and size of brain granulomas in each group. H37Rv i.c.vent.-infected mice had significantly more granulomas which were larger compared to H37Rv i.v.-infected mice (Figure 5e and f). Median (IQR) granuloma size was 1.18 (0.85-2.18) mm^2 in H37Rv i.c.vent.-infected mice compared to 0.07 (0.03-0.10) mm^2 in H37Rv i.v.-infected mice (p = 0.0022). Analysis of the adhesion molecules showed that ICAM-1 was significantly increased in i.c.vent.-infected mice relative to i.v.-infected mice (Figure 5g). P-selectin in H37Rv-infected mice was similarly upregulated in both routes of infection compared to saline controls (p = 0.0022) (Figure 5h). The higher ICAM-1 expression may explain the increased infiltration of leukocytes which in turn lead to larger granuloma size in the H37Rv i.c.vent.-infected compared to H37Rv i.v.-infected mice.

A similar trend was observed for CDC1551 *M.tb* strain. CDC1551 i.c.vent.-infected mice had a higher histopathological score than i.v.-infected mice (Supplementary Table 1), although the number of brain granulomas was similar for both routes of infection with this *M.tb* strain (Supplementary figure 6a). The median (IQR) granuloma size in i.c.vent. route of 0.49 (0.43-0.74) mm^2 was significantly larger than the i.v. route of 0.06 (0.01-0.17) mm^2 (p = 0.0022) (Supplementary figure 6b), with corresponding increase of ICAM-1 expression in the i.c.vent-infected compared to the i.v.-infected mice (Supplementary 6c). In contrast, p-selectin expression was lower in the i.c.vent-infected mice (Supplementary 6d).

These findings again indicated that while i.v.-infected mice were capable of developing CNS-TB, the i.c.vent route resulted in a more compartmentalized immunopathological response.

bioRxiv preprint doi: https://doi.org/10.1101/2021.08.15.456427; this version posted August 16, 2021. The copyright holder for this preprint (which was not certified by peer review) is the author/funder, who has granted bioRxiv a license to display the preprint in perpetuity. It is made available under aCC-BY-NC-ND 4.0 International license.

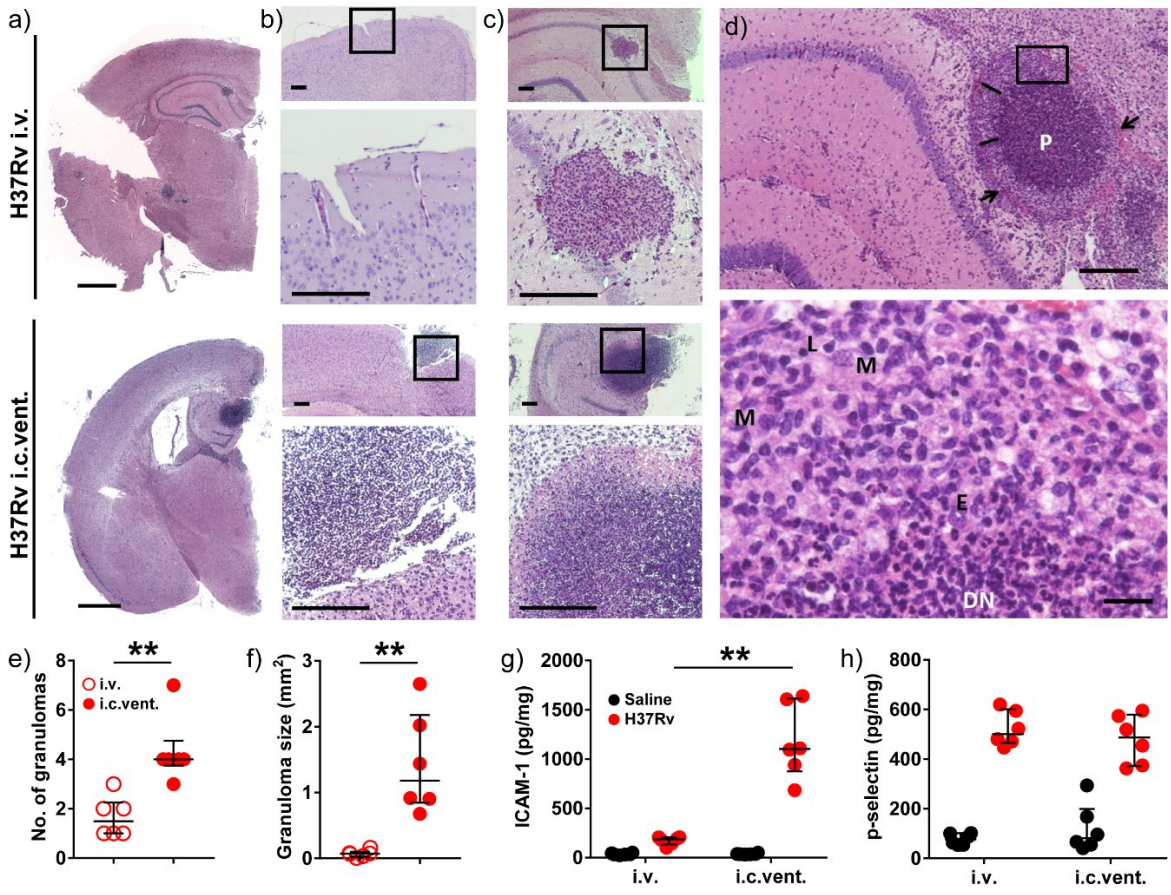

Figure 5. *Nos2*$^{-/-}$ mice infected with H37Rv by the i.c.vent. route developed pyogranulomas and larger granulomatous lesions with increased concentrations of ICAM-1 compared to i.v. route. (a) Overall histopathology via H&E stain demonstrate more severe (b) meningitis and (c) parenchymal granulomatous inflammation in H37Rv i.c.vent. than H37Rv i.v. mice. Bottom panel: high-power views of insets. (a) Scale bar = 1 mm. (b) and (c) Scale bar = 200 µm. (d) Well-formed pyogranuloma (P) in the hippocampus surrounded with sheets of inflammatory infiltrate (line) and covered with thin fibrous capsule (arrow). High-power view (inset) of the pyogranuloma shows presence of degenerating neutrophils (DN) at the centre, surrounded with macrophages (M), epithelioid cells (E) and few lymphocytes (L). Scale bar = 200 µm (20 µm in high-power view). Histology is representative of 6 mice. (e) and (f) H37Rv i.c.vent.- infected mice had more and larger brain granulomas. The number and size of granulomas in each group were respectively quantified from 6 different sections of 6 mice. H37Rv i.c.vent.-infected mice show higher levels of (g) ICAM-1 compared to i.v.-infected mice, whereas (h) p-selectin levels were comparable. Bars represent median and IQR. Statistical analysis was conducted using Mann-Whitney test. **, $p < 0.01$.

bioRxiv preprint doi: https://doi.org/10.1101/2021.08.15.456427; this version posted August 16, 2021. The copyright holder for this preprint (which was not certified by peer review) is the author/funder, who has granted bioRxiv a license to display the preprint in perpetuity. It is made available under aCC-BY-NC-ND 4.0 International license.

Table 1. Histopathological evaluation of *M.tb*-induced lesions in H37Rv-infected mice

Lesions*	H37Rv i.v.				H37Rv i.c.vent.			
	M	C	H	T	M	C	H	T
Inflammation (MNCs)	0	0	0	0	1	3	2	0
Perivascular cuffing		0	0	0		3	2	2
Gliosis		1	1	0		3	1	0
Granuloma		1	2	0		2	0	0
Pyrogranuloma		0	0	0		4	3	0
Neuronal degeneration/necrosis		0	0	0		2	1	0
Liquefactive necrosis (+/-)§		+	+	-		+	+	-
Presence of bacilli (+/-)§	-	-	+	-	-	+	+	-

M: meninges; C: cerebral cortex; H: hippocampus; T: thalamus

*Severity of lesions in each group are scored on a scale of 0–5: 0 – no abnormalities detected; 1 – minimal; 2 – mild; 3: moderate; 4: marked; 5: severe. The average score of 5–6 mice per group is shown.

§+/-: present/absent

bioRxiv preprint doi: https://doi.org/10.1101/2021.08.15.456427; this version posted August 16, 2021. The copyright holder for this preprint (which was not certified by peer review) is the author/funder, who has granted bioRxiv a license to display the preprint in perpetuity. It is made available under aCC-BY-NC-ND 4.0 International license.

H37Rv i.c.vent.-infected mice have higher expression of pro-inflammatory cytokines, Th1 chemokines and neutrophil chemoattractants

Inflammatory cytokines found upregulated in the CSF of TBM patients included TNF-α, IFN-γ, IL-1β and IL-6 (Misra et al., 2010; Nagesh Babu, Kumar, Kalita, & Misra, 2008). To determine if our model has a similar CNS immunological phenotype as human TBM patients, we analysed the expression of pro-inflammatory cytokines in the brain.

Pro-inflammatory cytokines TNF-α, IFN-γ, IL-1β and IL-6 were significantly increased by 17.8-fold, 31.0-fold, 4.8-fold and 7.1-fold, respectively in H37Rv i.c.vent. compared to H37Rv i.v.-infected mice (Figure 6a-d; all $p < 0.01$), and were observed in both *M.tb* strains (Supplementary Figure 7a-d). In addition, H37Rv i.c.vent.-infected mice demonstrated 31.7-fold, 7.3-fold, 6.2-fold and 56.8-fold higher expression of Th1 chemokines CCL-3, -4, -5 and CXCL-10 than H37Rv i.v.-infected mice respectively (Figure 6e-h; all $p < 0.01$). This was also observed with the CDC1551 strain (Supplementary Figure 7e-h). The higher concentration of pro-inflammatory cytokines and Th1 chemokines in i.c.vent. mice may explain the more pronounced inflammation and greater extent of inflammatory cell infiltration around cerebral blood vessels in i.c.vent.-infected compared to i.v.-infected mice.

Neutrophil chemokines CXCl-1, CXCL-2 and LIX were upregulated by 1.4-fold, 35.6-fold and 5.2-fold, respectively in H37Rv i.c.vent.-infected than H37Rv i.v.-infected mice (Figure 6i-k). While CXCL-1 expression was similar between the two infection routes of CDC1551-infected mice, CDC1551 i.c.vent. mice had higher expression of CXCL-2 and LIX than CDC1551 i.v. mice (Supplementary figure 7i-k). The significantly higher expression of neutrophil chemoattractants in i.c.vent.-infected mice, independent of *M.tb* strains, may explain the

bioRxiv preprint doi: https://doi.org/10.1101/2021.08.15.456427; this version posted August 16, 2021. The copyright holder for this preprint (which was not certified by peer review) is the author/funder, who has granted bioRxiv a license to display the preprint in perpetuity. It is made available under aCC-BY-NC-ND 4.0 International license.

presence of pyogranulomas with marked neutrophilic infiltration in i.c.vent.- but not i.v.-infected mice.

Collectively, these immunological findings indicate that i.c.vent. infection of *Nos2*$^{-/-}$ mice with H37Rv strain creates a better CNS-TB model than the i.v. route of infection as it exhibited more pronounced brain inflammation as shown by the higher expression of pro-inflammatory cytokines, Th1 chemokines and neutrophil chemoattractants.

bioRxiv preprint doi: https://doi.org/10.1101/2021.08.15.456427; this version posted August 16, 2021. The copyright holder for this preprint (which was not certified by peer review) is the author/funder, who has granted bioRxiv a license to display the preprint in perpetuity. It is made available under aCC-BY-NC-ND 4.0 International license.

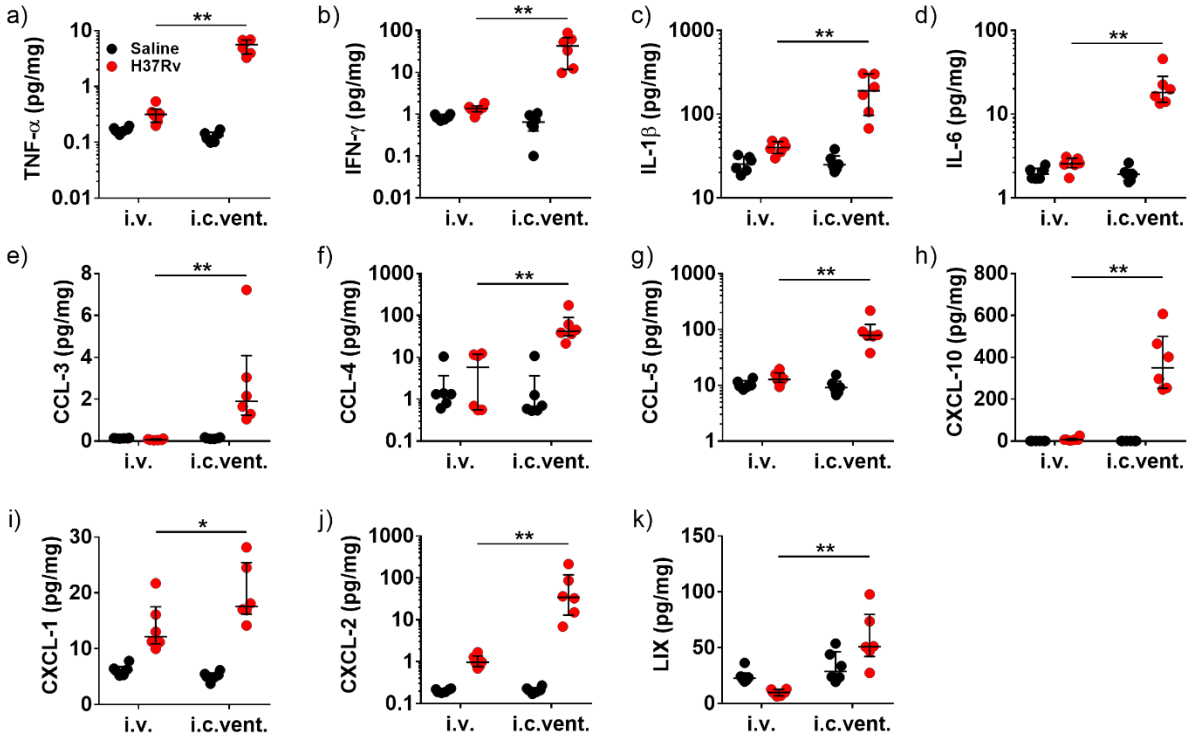

368

369 **Figure 6. H37Rv infection by the i.c.vent. route resulted in significantly higher brain expression**
370 **of inflammatory mediators than the i.v. route.** H37Rv i.c.vent.-infected mice had higher
371 concentrations of (a-d) pro-inflammatory cytokines, (e-h) Th1 chemokines, and (i-k) neutrophil
372 chemoattractants than H37Rv i.v. mice. Concentrations of inflammatory mediators in the brain were
373 measured after day 21 p.i.. Concentration of each immunological marker was normalised against the
374 total protein concentration. Bars represent median and interquartile ranges. Statistical analysis was
375 conducted using Mann-Whitney test. *, $p < 0.05$; **, $p < 0.01$.

376

bioRxiv preprint doi: https://doi.org/10.1101/2021.08.15.456427; this version posted August 16, 2021. The copyright holder for this preprint (which was not certified by peer review) is the author/funder, who has granted bioRxiv a license to display the preprint in perpetuity. It is made available under aCC-BY-NC-ND 4.0 International license.

DISCUSSION

Human CNS TB is severe and progress is limited by lack of good animal model systems that reflect immunopathology in human CNS TB. Our study determined the effects of mouse strain, *M.tb* strain and route of infection on the development of a murine CNS-TB model with human-like pathology. Here, we show that i.c.vent. infection of *Nos2*$^{-/-}$ mice with *M.tb* H37Rv makes a CNS-TB model that shares similar clinical features of human CNS-TB, including neurological morbidity, high mortality, and increased CNS expression of inflammatory mediators. Importantly, our model demonstrated histological evidence of parenchymal granulomas in the cerebral cortex, hippocampus and the presence of necrotizing granulomas similar to human CNS-TB tuberculomas (Chatterjee, 2011; P. R. Donald & Schoeman, 2009). The presence of a central area of liquefactive necrosis in pyogranulomas of H37Rv i.c.vent.-infected mice resembled human caseating tuberculomas with central liquefaction, a clinical feature that has not yet been replicated in existing murine CNS-TB models. Other features of human CNS-TB include perivascular infiltration with immune cells and a microglial reaction (Chatterjee, 2011; Saez-Llorens, Ramilo, Mustafa, Mertsola, & McCracken, 1990). Similar to that observed in humans, our CNS-TB model showed the presence of gliosis and perivascular cuffing throughout the brain parenchyma.

We evaluate the simultaneous expression of adhesion molecules, chemokines, and cytokines in an attempt to elucidate the mechanism underlying the chronic inflammatory state in human CNS-TB. While several clinical studies have unanimously demonstrated an increased CSF expression of inflammatory cytokines TNF-α, IFN-γ, IL-1β and IL-6 in TBM patients (Misra et al., 2010; Nagesh Babu et al., 2008; Sharma et al., 2017), current murine CNS-TB models have failed to recapitulate this immunological profile (Be et al., 2008; van Well et al., 2007).

bioRxiv preprint doi: https://doi.org/10.1101/2021.08.15.456427; this version posted August 16, 2021. The copyright holder for this preprint (which was not certified by peer review) is the author/funder, who has granted bioRxiv a license to display the preprint in perpetuity. It is made available under aCC-BY-NC-ND 4.0 International license.

Through immunological analysis, we showed that H37Rv i.c.vent.-infected *Nos2*$^{-/-}$ mice had significantly increased expression of TNF-α, IFN-γ, IL-1β and IL-6, similar to human TBM patients (Misra et al., 2010; Nagesh Babu et al., 2008), indicating that our pre-clinical model mirrors human CNS-TB. In addition, we demonstrated H37Rv i.c.vent.-infected mice exhibited upregulation of adhesion molecules p-selectin and ICAM-1 compared to saline controls, in keeping with the increased leukocyte infiltration in the brain and extends previous *in vitro* observations that *M.tb* increases expression of endothelial adhesion molecules in a co-culture BBB model (Brilha et al., 2017).

While i.c.vent. infection of *Nos2*$^{-/-}$ mice with either *M.tb* H37Rv or CDC1551 resulted in a high mortality (67% and 60% respectively), similar to human CNS-TB (Karstaedt, Valtchanova, Barriere, & Crewe-Brown, 1998; Porkert, Sotir, Parrott-Moore, & Blumberg, 1997), H37Rv is superior to CDC1551 as the murine CNS-TB model for two reasons. Firstly, H37Rv infection resulted in the development of more severe neurological deficits with a worse neurobehavioral score and earlier mortality than CDC1551 infection, which reflected the neurological morbidity and severity of disease in human CNS-TB (Christensen, Andersen, Thomsen, Andersen, & Johansen, 2011; Shaw, Pasipanodya, & Gumbo, 2010). Secondly, H37Rv-infected mice showed an increased severity of histopathological lesions than CDC1551-infected mice, demonstrated by the greater extent of pyogranulomas and liquefactive necrosis in H37Rv i.c.vent. mice, extending from the cerebral cortex to the hippocampus which were not observed in CDC1551-infected mice, but similar to human CNS-TB histology (Zaharie et al., 2020). This is consistent with previous findings where H37Rv is more virulent than CDC1551 in animal models of pulmonary TB both in rabbits (Bishai et al., 1999) and in mice (Manca et al., 1999).

bioRxiv preprint doi: https://doi.org/10.1101/2021.08.15.456427; this version posted August 16, 2021. The copyright holder for this preprint (which was not certified by peer review) is the author/funder, who has granted bioRxiv a license to display the preprint in perpetuity. It is made available under aCC-BY-NC-ND 4.0 International license.

Previous murine CNS-TB models have employed direct injection into the brain parenchyma to induce CNS infection (Mazzolla et al., 2002; Olin et al., 2008; Zucchi et al., 2012), which resulted either in granulomas being restricted to the injection site with no widespread inflammation or the absence of granulomas. Thus, to better mimic the rupture of the Rich foci in human CNS-TB, with the subsequent release of *M.tb* into the CSF to induce TBM (Rock et al., 2008), we inoculated *M.tb* into the third ventricle for meningeal infection. To prevent surgery-related loss of mice due to excessive bleeding or hemorrhage, we injected *M.tb* at an angle into the third ventricle to avoid puncturing the superior sagittal sinus. In addition to the direct CNS inoculation of *M.tb* via the i.c.vent. route, we also explored the i.v. route to mimic the natural course of hematogenous spread from the lung to the brain in human CNS-TB (Sanchez-Garibay, Hernandez-Campos, Tena-Suck, & Salinas-Lara, 2018). However, we found the i.v. route of infection to be less suited for our murine CNS-TB model, as the mice exhibited a widespread disseminated infection resembling miliary TB, with granulomas observed in multiple organs of the lungs, spleen, heart, and kidneys, but not typical brain lesions. Dissemination of *M.tb* to the heart of H37Rv i.v. mice may explain the early and uniform lethality with mortality of these mice by day 30 p.i..

Different mouse strains have different susceptibilities to *M.tb* infection, which may explain the varying degree of disease and brain histopathology in existing murine CNS-TB models. To investigate whether the C3HeB/FeJ mice, which are hypersusceptible to pulmonary TB infection (Irwin et al., 2015; Kramnik et al., 2000), or the *Nos2*$^{-/-}$ mice, which have an altered innate immune response, are more susceptible to CNS-TB infection, we evaluated the C3HeB/FeJ and *Nos2*$^{-/-}$ mouse strains for our murine CNS-TB model. *M.tb*-infected *Nos2*$^{-/-}$

bioRxiv preprint doi: https://doi.org/10.1101/2021.08.15.456427; this version posted August 16, 2021. The copyright holder for this preprint (which was not certified by peer review) is the author/funder, who has granted bioRxiv a license to display the preprint in perpetuity. It is made available under aCC-BY-NC-ND 4.0 International license.

mice exhibited worse neurobehavioral score than C3HeB/FeJ mice and developed neurological symptoms such as myoclonic jerks and limb weakness that resembled seizures and hemiparesis respectively in human CNS-TB patients (Rock et al., 2008). In addition, infected *Nos2*$^{-/-}$ mice demonstrated greater inflammatory cell infiltrates, higher expression of adhesion molecules and chemokines in the brain than C3HeB/FeJ mice. Although there was trend to lower mycobacterial load in the C3HeB/FeJ mice, these infected mice expressed similar level of adhesion molecules and chemokines in the brain to saline controls, indicating that the CNS response to infection in the C3HeB/FeJ mice was minimal. These findings show that *Nos2*$^{-/-}$ mice is a better CNS-TB model than C3HeB/FeJ mice, and underscores the role of *Nos2*-induced NO production in inhibiting *M.tb* growth in mice (Dallenga et al., 2018).

Altogether, i.c.vent. infection of *Nos2*$^{-/-}$ mice with H37Rv creates a murine CNS-TB model that best resembled human CNS-TB immunopathology, exhibiting the worst neurobehavioral score and with a high and early mortality reflecting disease severity and its associated neurological morbidity. In our study, extensive brain inflammation was seen with granulomas and pyogranulomas that resembled the granulomatous inflammation in human CNS-TB patients (Zaharie et al., 2020), with a corresponding increase in expression of adhesion molecules, Th1 cytokine response and neutrophil chemoattractants. As this model replicates the histopathological features of human CNS-TB, it is particularly useful for future drug studies to assess the penetration of potential drug candidates into CNS-TB tuberculomas, and evaluate their efficacy in reducing immunopathology and consequently improve neurological outcome in CNS-TB.

bioRxiv preprint doi: https://doi.org/10.1101/2021.08.15.456427; this version posted August 16, 2021. The copyright holder for this preprint (which was not certified by peer review) is the author/funder, who has granted bioRxiv a license to display the preprint in perpetuity. It is made available under aCC-BY-NC-ND 4.0 International license.

MATERIALS AND METHODS

All animal procedures were approved by the Institutional Animal Care and Use Committee of National University of Singapore under protocol R15-1068, in accordance with national guidelines for the care and use of laboratory animals for scientific purposes.

Bacterial strains and growth conditions for infection

Mycobacterium tuberculosis (*M.tb*) strains H37Rv and CDC1551 were kindly provided by Professor Nick Paton and Associate Professor Sylvie Alonso (both NUS, Singapore) respectively. For infection experiments, a frozen vial of *M.tb* was thawed and cultured to mid-logarithmic phase at an optical density of 0.6-0.8. Prior to infection, the *M.tb* was centrifuged at 3,200 x g for 10 minutes and resuspended in 1 mL sterile 0.9% NaCl. The *M.tb* inoculum was then plated to determine the dose of infection.

Mouse cannula implantation and infection

Six- to eight-week-old male C57BL/6 *Nos2*$^{-/-}$ and C3HeB/FeJ mice (Jackson Laboratory, Bar Harbor, Maine) were used for intra-cerebroventricular (i.c.vent.) or intravenous (i.v.) infection. Mice in the i.c.vent. group were cannulated one week before infection. An illustration of the stereotaxic coordinates of site of injection and the positioning of guide cannula is shown in Supplementary Figure 1a. A motorized stereotaxic instrument (Neurostar, Tübingen, Germany) was used to implant a 26-gauge guide cannula (RWD, Shenzhen, China) into the third ventricle (coordinates from the bregma: -1.6 mm posterior, 0 mm lateral, -2.5 mm ventral). Mice were injected with 0.5 µL of sterile 0.9% NaCl or 2×10^8 CFU/mL *M.tb* through the brain cannula (over 5 min) using the syringe pump (Harvard Apparatus, Holliston, Massachusetts). Mice in the i.v. group were injected with 50 µL of sterile 0.9% NaCl or 2×10^6 CFU/mL *M.tb* via the

bioRxiv preprint doi: https://doi.org/10.1101/2021.08.15.456427; this version posted August 16, 2021. The copyright holder for this preprint (which was not certified by peer review) is the author/funder, who has granted bioRxiv a license to display the preprint in perpetuity. It is made available under aCC-BY-NC-ND 4.0 International license.

retro-orbital sinus. All mice were observed for mortality and weight change. Humane endpoints included ≥ 20% weight loss, complete hind limb paralysis and repeated seizures. Infected mice were also monitored daily for 56 days after infection for clinical signs indicative of CNS-TB, such as limb weakness, tremors, and twitches.

Trypan blue was administered into four cannulated mice and the brains harvested 15 mins post-administration to allow for distribution of the dye in both right and left cerebral hemispheres. A sagittal illustration of the ventricular system in the mouse brain, which include the lateral ventricles, third ventricle and aqueduct that leads to the fourth ventricle, is depicted in Supplementary Figure 1b. Coronal sections of each brain verifies that the dye is in the ventricular system (Supplementary figure 1c), indicating successful brain cannulation into the third ventricle. *Nos2*$^{-/-}$ or C3HeB/FeJ mice were infected with *M.tb* 7 days after brain cannulation, and the blood, brain, lungs, liver and spleen were harvested 56 days post-infection (p.i.) for enumeration of mycobacterial load, histopathological analysis and immunological marker analysis (Supplementary figure 1d).

Neurobehavioral scoring

Neurobehavioral scoring was performed by a researcher (P.X.Y.) blinded to the route of infection and strain of *M.tb* according to a scoring list for CNS-TB mouse model (Table 2), adapted from Tucker et al (Tucker et al., 2016). Each scoring parameter ranged from one, corresponding to no abnormalities, to a variable maximum score. The minimum total score is 3 indicating a normal mouse. Higher neurological scores reflect an increasing severity of neurological deficits with a maximum total score of 7.

bioRxiv preprint doi: https://doi.org/10.1101/2021.08.15.456427; this version posted August 16, 2021. The copyright holder for this preprint (which was not certified by peer review) is the author/funder, who has granted bioRxiv a license to display the preprint in perpetuity. It is made available under aCC-BY-NC-ND 4.0 International license.

Table 2. Composite neurobehavioral score criteria for CNS-TB mouse model

Criteria	Score
Tremors	
Absent	1
Present	2
Twitch/jerk	
Absent	1
Mild (< 3 in 10 sec)	2
Severe (≥ 3 in 10 sec)	3
Eyes	
Normal	1
Closed eyelids	2

Organ harvesting and processing

Eight weeks post-infection, mice were deeply anesthetized before cardiac puncture was performed for blood collection. The brain, lungs, liver and spleen were harvested and the gross pathology examined before tissue processing. Half of each organ was fixed in 10% neutral buffered saline for histology, while the other half was homogenized for bacterial enumeration and characterization of immunological markers. Organs were homogenized by high-speed shaking in 2 mL microcentrifuge tubes filled with sterile PBS and 5/7 mm stainless steel beads using TissueLyser LT (Qiagen, Hilden, Germany).

Histopathological analysis

Histopathology was performed on the left hemisphere of the brain. The murine brain was fixed in 10% neutral buffered saline, paraffin embedded and sectioned to 4 µm thickness. Brain slices were stained with hematoxylin-eosin (H&E) (Vector Laboratories, Burlingame, California) to characterise pathological lesions and Ziehl-Neelson staining (Sigma-Aldrich, St. Louis, Missouri) to detect mycobacterium according to manufacturer's instructions. Histopathological examination was carried out in a blinded fashion by a histopathologist (R.R.) based on the presence of pathological changes including inflammation, perivascular cuffing, gliosis,

bioRxiv preprint doi: https://doi.org/10.1101/2021.08.15.456427; this version posted August 16, 2021. The copyright holder for this preprint (which was not certified by peer review) is the author/funder, who has granted bioRxiv a license to display the preprint in perpetuity. It is made available under aCC-BY-NC-ND 4.0 International license.

neuronal necrosis, granuloma, pyogranuloma and necrosis. Definition of granulomatous lesions in this study includes both granulomas and pyogranulomas. Grading of severity was assigned on the following scale: 0: no abnormalities detected; 1-minimal; 2-mild; 3-moderate; 4-marked & 5-severe. The total number and area of granulomatous lesions were measured from 6 different sections of 5-6 mice. To quantify the area of granuloma, we utilized the free-hand tool in ImageJ (NIH, Bethesda, Maryland) and manually demarcated the granuloma as a region of interest for area measurement.

Immunological marker analysis

Adhesion molecules, cytokines and chemokines were analysed by Fluorokine multianalyte profiling kit according to the manufacturer's protocol (R&D Systems, Minneapolis, Minnesota) on the Bio-Plex 200 platform (Bio-Rad, Hercules, California). The minimum detection limit for the ICAM-1 and p-selectin were 52.7 pg/ml and 2.6 pg/ml respectively. The minimum detection limit for the cytokines and chemokines were CCL-2/MCP-1 134 pg/ml, CCL-3/MIP-1α 0.452 pg/ml, CCL-4/ MIP-1β 77.4 pg/ml, CCL-5/ RANTES 19.1 pg/ml, CCL-7/ MCP-3 1.69 pg/ml, CCL-8/ MCP-2 0.283 pg/ml, CCL-11/Eotaxin 1.46 pg/m, CCL-12/ MCP-5 0.613 pg/ml, CCL-19/ MIP-3β 2.28 pg/ml, CCL-20/ MIP-3α 3.95 pg/ml, CCL-22/ MDC 0.965 pg/ml, CXCL-1/ KC 32.9 pg/ml, CXCL-2/ MIP-2 1.97 pg/ml, CXCL-10/ IP-10 6.85 pg/ml, CXCL-13/ BLC 19.3 pg/ml, IL-1α 8.17 pg/ml, IL-1β 41.8 g/ml, IL-6 2.30 pg/ml, IL-12 p70 12.8 pg/ml, IL-17A7.08 pg/ml, IL-27 1.84 pg/ml, LIX 2.02 pg/ml, TNF-α 1.47 pg/ml, IFN-γ 1.85 pg/ml. Brain homogenates were assayed at neat for all analytes and results were normalised to their total protein concentrations (Bio-Rad, Hercules, California).

Statistical analysis

bioRxiv preprint doi: https://doi.org/10.1101/2021.08.15.456427; this version posted August 16, 2021. The copyright holder for this preprint (which was not certified by peer review) is the author/funder, who has granted bioRxiv a license to display the preprint in perpetuity. It is made available under aCC-BY-NC-ND 4.0 International license.

Continuous variables are presented as medians and interquartile range. Neurobehavior scores between groups were compared using two-way ANOVA with post-hoc Tukey's multiple comparisons test. Levels of adhesion molecules, cytokines and chemokines, and CFU counts between groups were compared using Mann-Whitney test. Comparison of survival curves between groups was calculated using the log-rank test. A two-sided value of $p < 0.05$ was considered significant. All analyses were performed using GraphPad Prism version 7.05 (Graphpad, San Diego, California).

bioRxiv preprint doi: https://doi.org/10.1101/2021.08.15.456427; this version posted August 16, 2021. The copyright holder for this preprint (which was not certified by peer review) is the author/funder, who has granted bioRxiv a license to display the preprint in perpetuity. It is made available under aCC-BY-NC-ND 4.0 International license.

Supplementary table 1. Histopathological evaluation of *M.tb*-induced lesions in CDC1551-infected mice

Lesions*	CDC1551 i.v.				CDC1551 i.c.vent.			
	M	C	H	T	M	C	H	T
Inflammation (MNCs)	0	0	0	0	3	3	1	0
Perivascular cuffing		0	0	0		2	2	1
Gliosis		0	0	0		2	1	0
Granuloma		0	1	0		2	0	0
Pyrogranuloma		0	0	0		3	0	0
Neuronal degeneration/necrosis		0	0	0		2	1	0
Liquefactive necrosis (+/-)§		-	-	-		+	-	-
Presence of bacilli (+/-)§	-	-	+	-	-	+	-	-

M: meninges; C: cerebral cortex; H: hippocampus; T: thalamus

*Severity of lesions in each group are scored on a scale of 0–5: 0 – no abnormalities detected; 1 – minimal; 2 – mild; 3: moderate; 4: marked; 5: severe. The average score of 5–6 mice per group is shown.

§+/-: present/absent

bioRxiv preprint doi: https://doi.org/10.1101/2021.08.15.456427; this version posted August 16, 2021. The copyright holder for this preprint (which was not certified by peer review) is the author/funder, who has granted bioRxiv a license to display the preprint in perpetuity. It is made available under aCC-BY-NC-ND 4.0 International license.

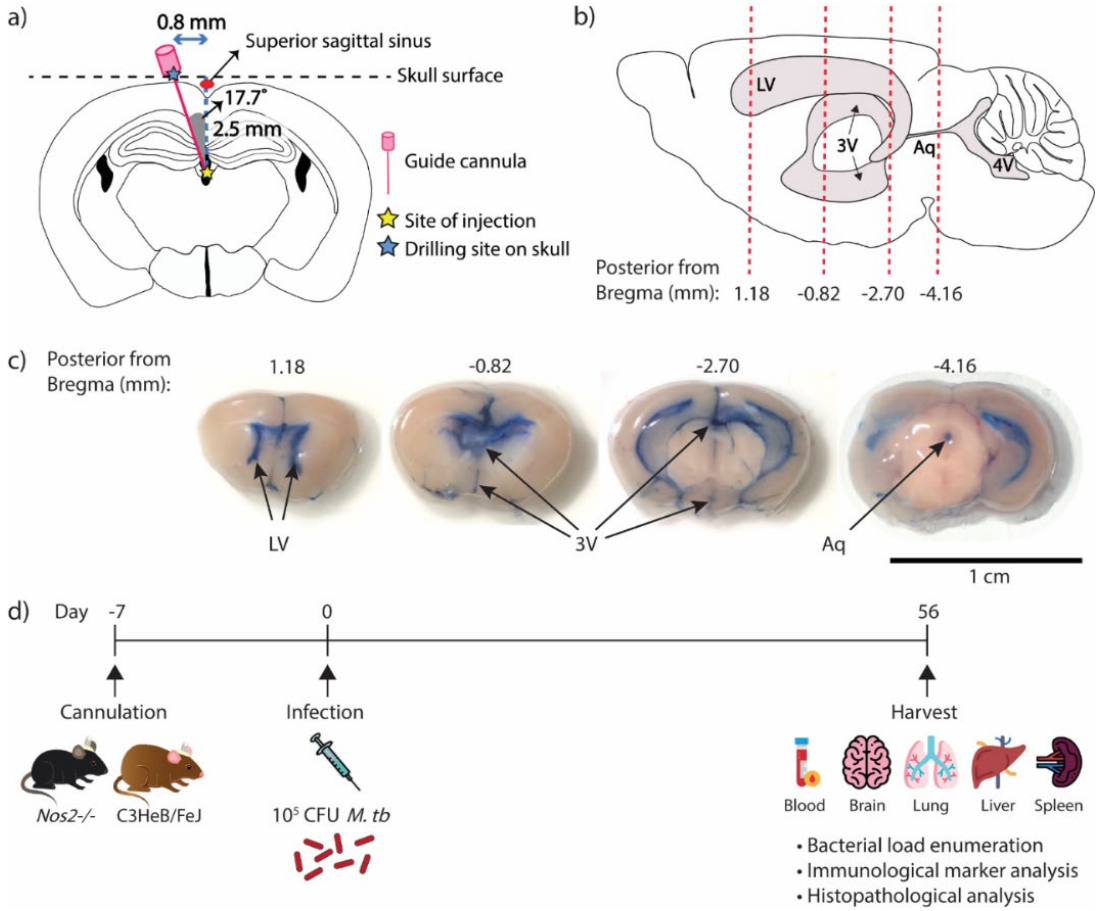

Supplementary figure 1. Cannula implantation and experimental timeline. (a) A schematic representation (coronal section) of the angled cannulation conducted for injection in the third ventricle. Stereotaxic coordinates for injection site from bregma: -1.60 mm posterior, 0 mm lateral, -2.50 mm ventral. Coordinates for drilling site on skull from bregma: -1.60 mm posterior, 0.80 mm lateral (left). Guide cannula is inserted at an angle of 17.7^{O}. (b) A schematic representation (sagittal section) of the ventricular system in the mouse brain showing the approximate positions of the lateral ventricle (Zucchi et al.), third-ventricle (3V), fourth-ventricle (4V) and aqueduct (Aq). The 4 dotted lines indicate the approximate location of the brain images shown in (c) with the stereotaxic coordinates posterior from Bregma annotated below. (c) Images of coronal sections of the brain after trypan blue dye administration. If cannula is successfully implanted in the third ventricle, the trypan blue dye will be distributed throughout the ventricular system as demonstrated in the four brain coronal sections. Images shown are representative of four cannulated mice. (d) A schematic representation of the experimental timeline for mice infected with *Mycobacterium tuberculosis* (*M.tb*) via the intra-cerebroventricular route.

bioRxiv preprint doi: https://doi.org/10.1101/2021.08.15.456427; this version posted August 16, 2021. The copyright holder for this preprint (which was not certified by peer review) is the author/funder, who has granted bioRxiv a license to display the preprint in perpetuity. It is made available under aCC-BY-NC-ND 4.0 International license.

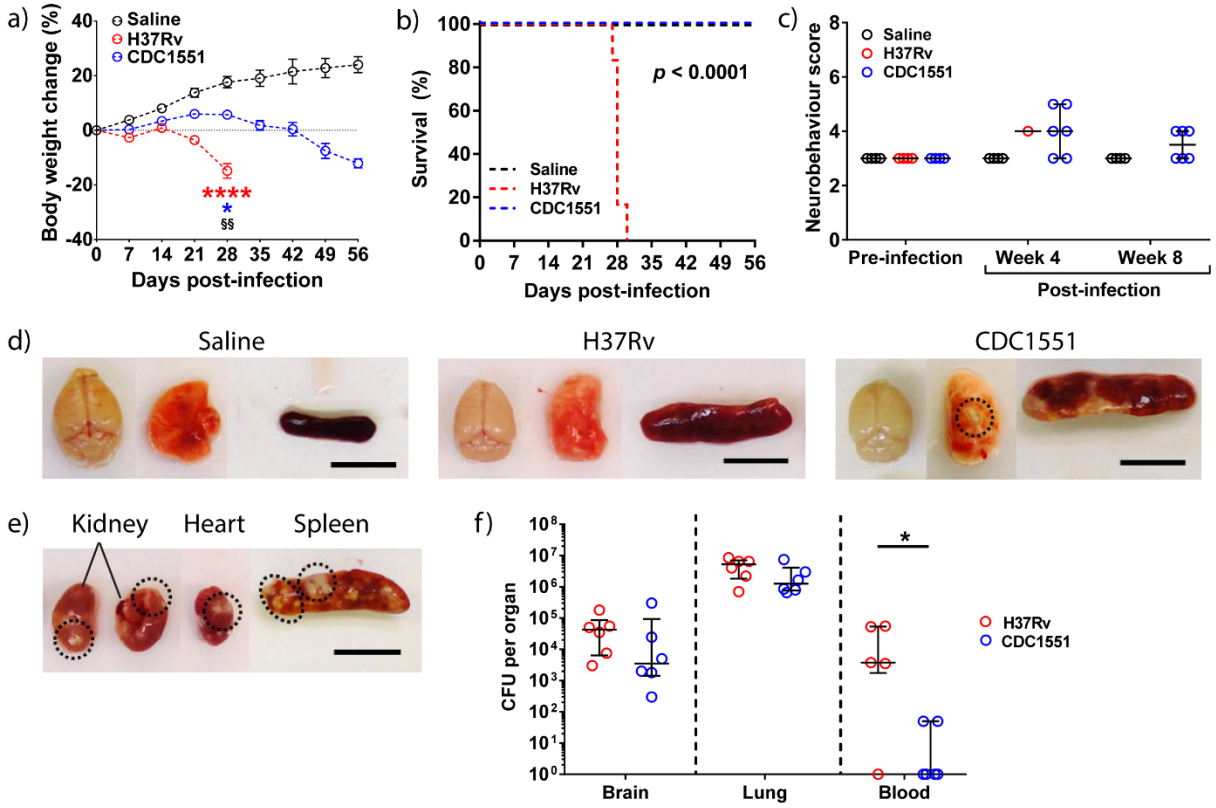

Supplementary figure 2. *Nos2*$^{-/-}$ mice infected with *M.tb* via the i.v. route demonstrate disseminated granulomas with mycobacteraemia in 50% of mice. (a) *M.tb*-infected mice lost significantly more weight than saline control. At day 28 p.i., H37Rv i.v. mice lost more weight than CDC1551 i.v. mice (§§). Percentage change in body weight relative to initial body weight at day 0 p.i. is shown. Bars represent mean ± SEM. *, $p < 0.05$; §§, $p < 0.01$; ****, $p < 0.0001$. Statistical analysis between H37Rv-infected mice and saline controls in red asterisks, while comparisons between CDC1551-infected mice and saline controls in blue asterisks. (b) Kaplan-Meier curve shows a significant difference in survival between the groups. (c) I.v.-infected mice demonstrate similar neurobehavioral score at 4 weeks p.i.. No data is available for H37Rv i.v. at 8 weeks p.i. as all mice died or reached humane endpoints by day 30 p.i.. (d) CDC1551 i.v.-infected mice developed granulomas (circled) in the lungs. Gross pathological examination of the brain, lung and spleen 21 days after infection. Images are representative of 5-6 mice per condition. (e) Granulomas (circled) are present in the kidneys, heart and spleen of i.v.-infected mice. Scale bars represent 1 cm. (f) H37Rv-infected mice demonstrate increased mycobacteraemia, while brain and lung CFU were comparable to CDC1551-infected mice. Bars represent median and IQR.

bioRxiv preprint doi: https://doi.org/10.1101/2021.08.15.456427; this version posted August 16, 2021. The copyright holder for this preprint (which was not certified by peer review) is the author/funder, who has granted bioRxiv a license to display the preprint in perpetuity. It is made available under aCC-BY-NC-ND 4.0 International license.

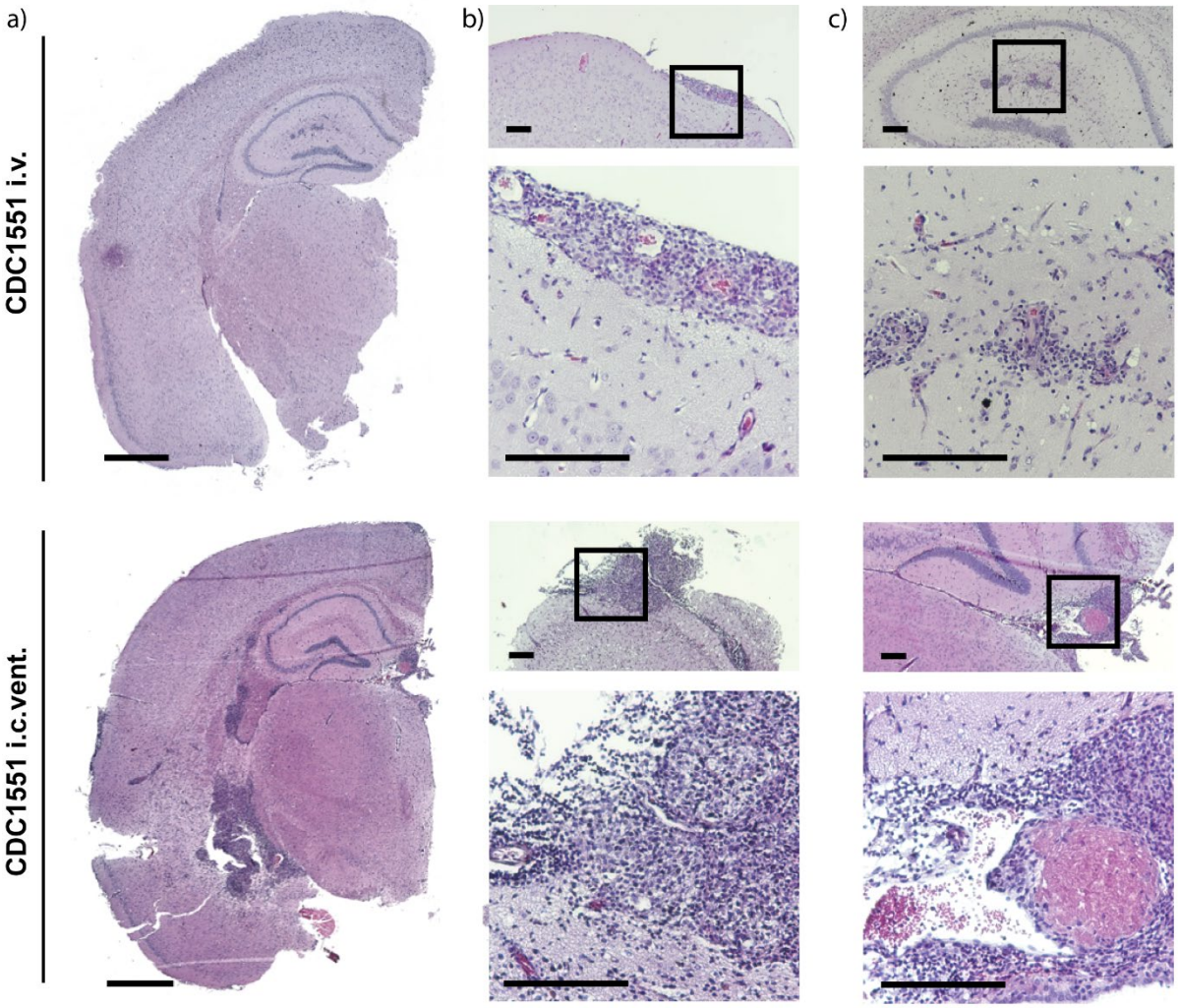

Supplementary figure 3. *Nos2*$^{-/-}$ mice infected with CDC1551 by the i.c.vent. route had more severe meningitis and granulomas compared to i.v. route. (a) Overall histopathology, (b) meningeal inflammation and (c) parenchymal granulomas are shown. Bottom panel: high-power views of insets. Histology is representative of 5-6 mice. (a) Scale bar = 1 mm. (b) and (c) Scale bar = 200 µm.

bioRxiv preprint doi: https://doi.org/10.1101/2021.08.15.456427; this version posted August 16, 2021. The copyright holder for this preprint (which was not certified by peer review) is the author/funder, who has granted bioRxiv a license to display the preprint in perpetuity. It is made available under aCC-BY-NC-ND 4.0 International license.

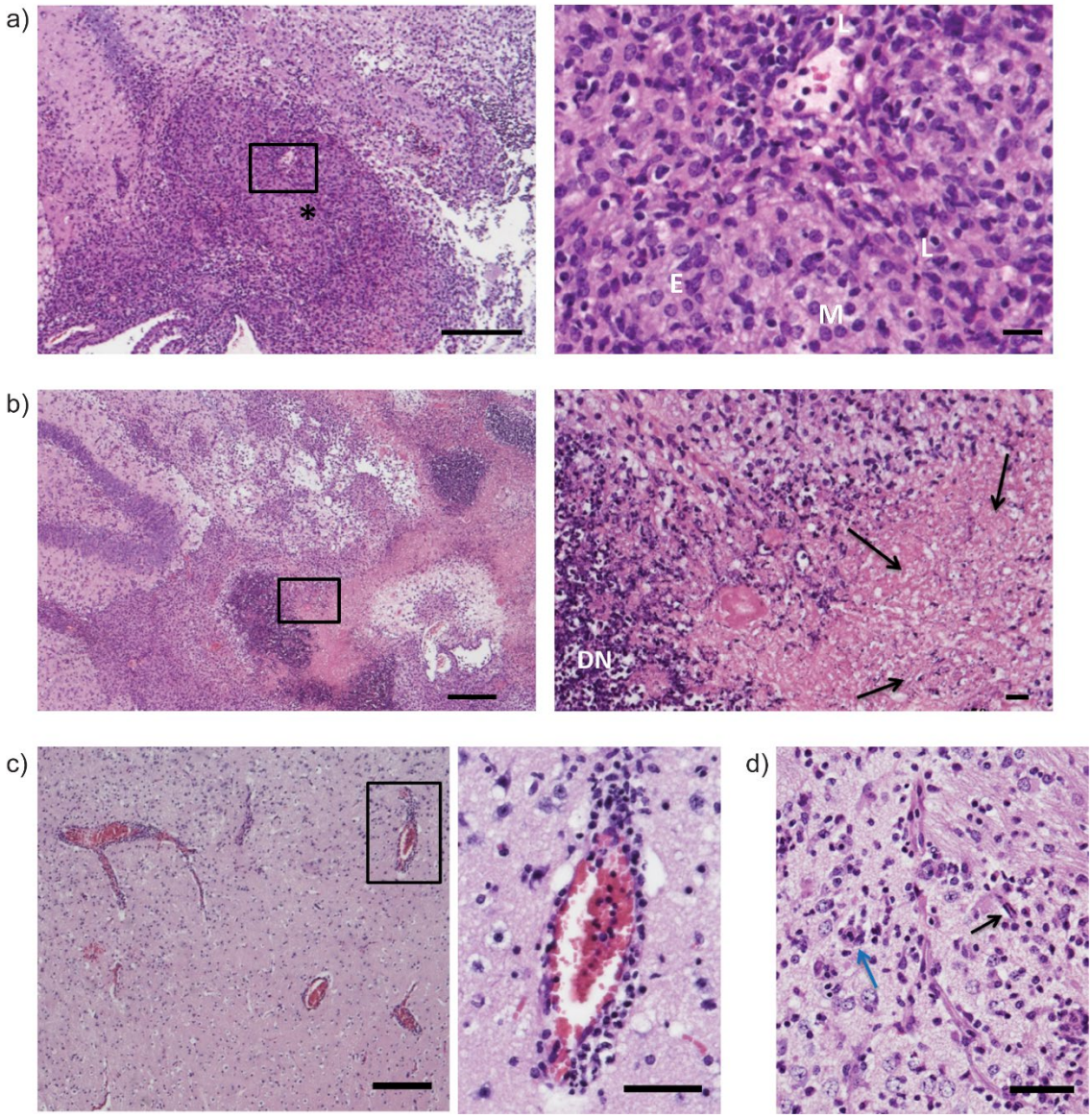

Supplementary figure 4. Pathological lesions in the brain of H37Rv i.c.vent.-infected mice. (a) Granuloma (*) present in the ventricle. High-power view (inset) of the granuloma demonstrates presence of macrophages (M), epithelioid cells (E) and few lymphocytes (L). Scale bar = 200 µm (20 µm in high-power view). (b) Pyogranuloma at the hippocampus showed a central area of liquefactive necrosis. High-power view (inset) of the area of liquefactive necrosis demonstrates eosinophilic cellular debris (arrow) with adjoined degenerating neutrophils (DN). Scale bar = 200 µm (50 µm in high-power view) (c) Prominent perivascular cuffing at multiple locations in the thalamus. High-power view (inset) displays inflammatory cell infiltration around a blood vessel. Scale bar = 200 µm (50 µm in high-power view) (d) Gliosis (black arrow) and neuronal necrosis present with pyknotic nucleus and eosinophilic cytoplasm (blue arrow). Scale bar = 50 µm. Histology representative of 6 mice.

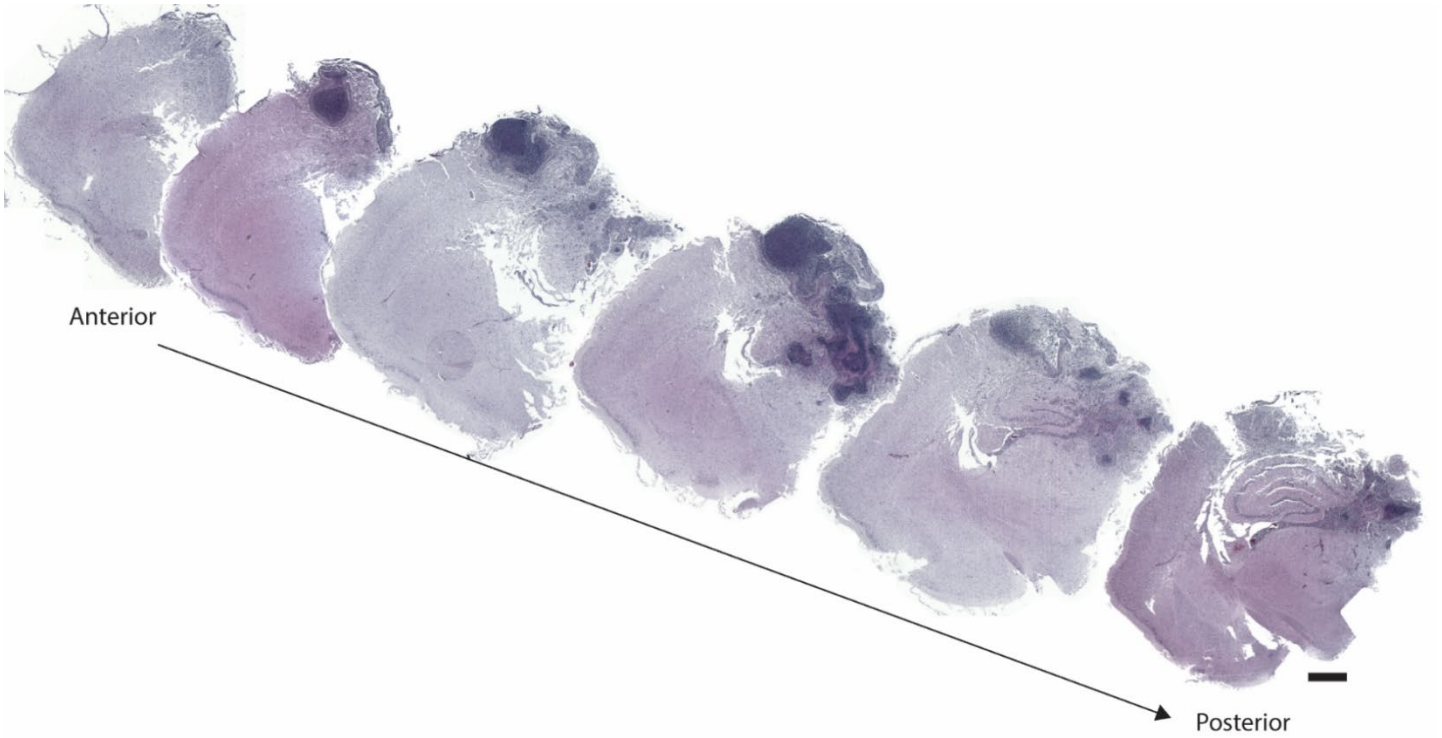

626

627 **Supplementary figure 5. Extensive meningeal and parenchymal inflammation are observed in the brain of *Nos2*$^{-/-}$ mice infected with H37Rv by the**
628 **i.c.vent. route.** Serial H&E-stained histopathological sections (each 500 µm apart) of the brain from the same animal shows the granuloma development in the
629 anterior-posterior axis. Scale bar = 1 mm. Histology representative of 5-6 mice.

630

bioRxiv preprint doi: https://doi.org/10.1101/2021.08.15.456427; this version posted August 16, 2021. The copyright holder for this preprint (which was not certified by peer review) is the author/funder, who has granted bioRxiv a license to display the preprint in perpetuity. It is made available under aCC-BY-NC-ND 4.0 International license.

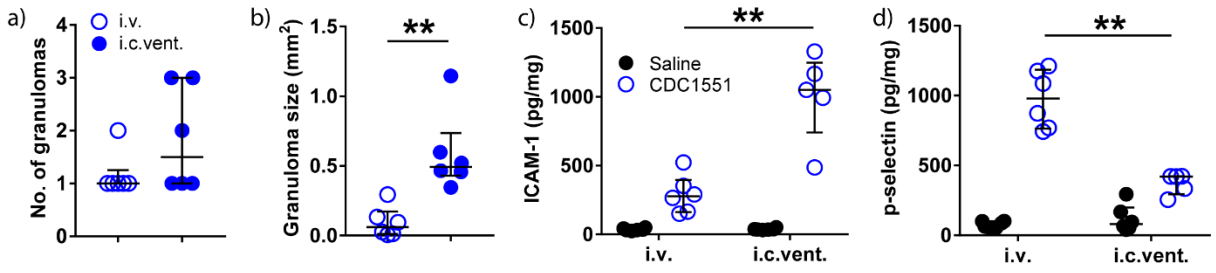

Supplementary figure 6. CDC1551 i.c.vent. mice had larger granulomas with increased concentration of adhesion molecule ICAM-1 than CDC1551 i.v. mice. (a) CDC1551-infected mice by the two routes of infection demonstrate similar number of brain granulomas. (b) CDC1551 i.c.vent.-infected mice had larger granulomas than CDC1551 i.v.-infected mice. The number and size of granulomas in each group were respectively quantified from 6 different sections of 5-6 mice. CDC1551 i.c.vent.-infected mice show higher expression of (c) ICAM-1 compared to i.v.-infected mice, whereas (d) p-selectin expression was higher in i.v.-infected than i.c.vent.-infected mice. Bars represent median and IQR. Statistical analysis was conducted using Mann-Whitney test. **, $p < 0.01$.

bioRxiv preprint doi: https://doi.org/10.1101/2021.08.15.456427; this version posted August 16, 2021. The copyright holder for this preprint (which was not certified by peer review) is the author/funder, who has granted bioRxiv a license to display the preprint in perpetuity. It is made available under aCC-BY-NC-ND 4.0 International license.

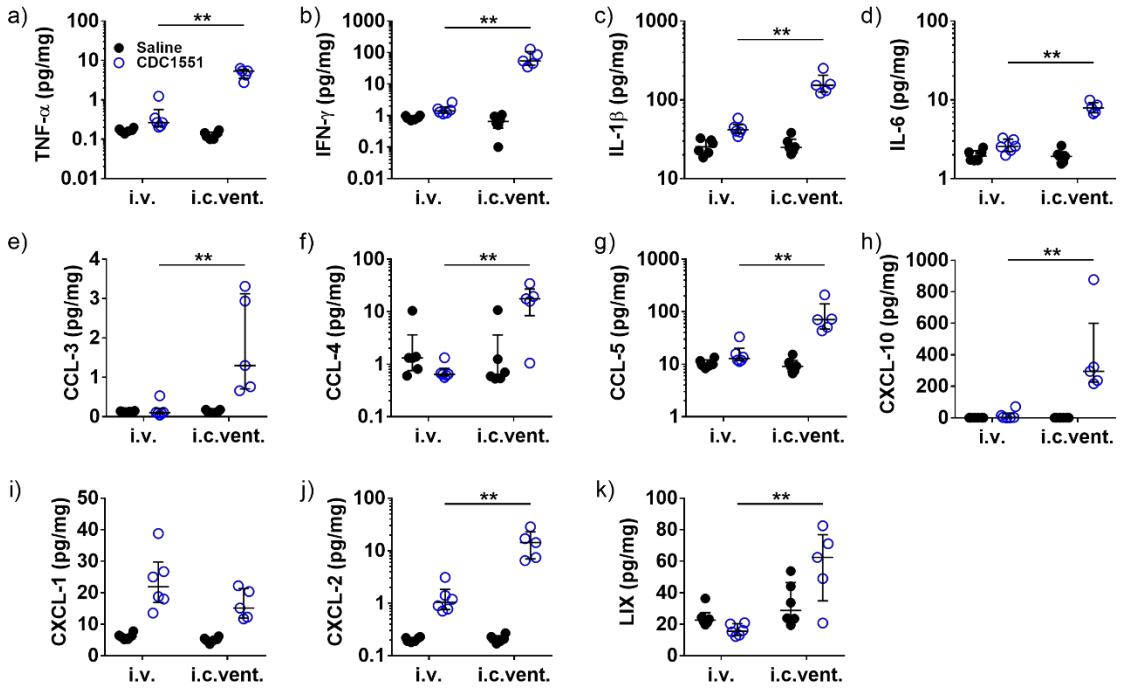

Supplementary figure 7. CDC1551 infection by the i.c.vent. route resulted in significantly higher brain expression of inflammatory mediators than i.v. route. CDC1551 i.c.vent.-infected mice had higher expression of (a-d) pro-inflammatory cytokines and (e-h) Th1 chemokines than CDC1551 i.v. mice. Among neutrophil chemoattractants, (i) CXCL-1 expression was similar between the two infection routes, while (j) CXCL-2 and (k) LIX were significantly increased in CDC1551 i.c.vent. than CDC1551 i.v. mice. Inflammatory mediators in the brain were measured after day 21 p.i.. Concentration of each immunological marker was normalised against the total protein concentration. Bars represent median and interquartile ranges. Statistical analysis was conducted using Mann-Whitney test. **, $p < 0.01$.

bioRxiv preprint doi: https://doi.org/10.1101/2021.08.15.456427; this version posted August 16, 2021. The copyright holder for this preprint (which was not certified by peer review) is the author/funder, who has granted bioRxiv a license to display the preprint in perpetuity. It is made available under aCC-BY-NC-ND 4.0 International license.

ACKNOWLEDGEMENTS

Catherine W. M. Ong is funded by Singapore National Medical Research Council (NMRC/TA/0042/2015, CSAINV17nov014; National University Health System (NUHS/RO/2017/092/SU/01, CFGFY18P11, NUHSRO/2020/042/RO5+5/ad-hoc/1), Singapore, iHealthtech at the National University of Singapore and recipient of the Young Investigator Award, Institut Merieux, Lyon, France. Xuan Ying Poh is supported by a postgraduate scholarship from the Yong Loo Lin School of Medicine, National University of Singapore. Jia Mei Hong was supported by NUSMed Post-Doctoral Fellowship (NUHSRO/2018/052/PDF/04). The authors would like to thank the operations team of the National University of Singapore BSL-3 core facility for the infrastructure and logistical support of the study. The authors would also like to thank National University of Singapore Comparative Medicine (CM) and the Neuroscience Phenotyping Core (NPC) for animal training and support. The authors are grateful to Professor Paul Elkington and Associate Professor Sylvie Alonso for commenting on the manuscript.

AUTHOR CONTRIBUTIONS

C.W.M.O. conceived the study. P.X.Y., H.J.M., M.Q.H. and C.W.M.O. designed the experiments. P.X.Y., H.J.M., M.Q.H., W.Y. and T.P.M. performed the experiments. P.X.Y., R.R. and C.W.M.O. analysed the data. P.X.Y. wrote the first draft of the manuscript.

COMPETING INTERESTS

The authors declare no competing interests.

bioRxiv preprint doi: https://doi.org/10.1101/2021.08.15.456427; this version posted August 16, 2021. The copyright holder for this preprint (which was not certified by peer review) is the author/funder, who has granted bioRxiv a license to display the preprint in perpetuity. It is made available under aCC-BY-NC-ND 4.0 International license.

REFERENCES

Be, N. A., Lamichhane, G., Grosset, J., Tyagi, S., Cheng, Q. J., Kim, K. S., . . . Jain, S. K. (2008). Murine model to study the invasion and survival of Mycobacterium tuberculosis in the central nervous system. *J Infect Dis, 198*(10), 1520-1528. doi:10.1086/592447

Bishai, W. R., Dannenberg, A. M., Jr., Parrish, N., Ruiz, R., Chen, P., Zook, B. C., . . . Pitt, M. L. (1999). Virulence of Mycobacterium tuberculosis CDC1551 and H37Rv in rabbits evaluated by Lurie's pulmonary tubercle count method. *Infect Immun, 67*(9), 4931-4934. doi:10.1128/IAI.67.9.4931-4934.1999

Bolin, C. A., Whipple, D. L., Khanna, K. V., Risdahl, J. M., Peterson, P. K., & Molitor, T. W. (1997). Infection of swine with Mycobacterium bovis as a model of human tuberculosis. *J Infect Dis, 176*(6), 1559-1566. doi:10.1086/514155

Brilha, S., Ong, C. W. M., Weksler, B., Romero, N., Couraud, P. O., & Friedland, J. S. (2017). Matrix metalloproteinase-9 activity and a downregulated Hedgehog pathway impair blood-brain barrier function in an in vitro model of CNS tuberculosis. *Sci Rep, 7*(1), 16031. doi:10.1038/s41598-017-16250-3

Chan, E. D., Chan, J., & Schluger, N. W. (2001). What is the role of nitric oxide in murine and human host defense against tuberculosis?Current knowledge. *Am J Respir Cell Mol Biol, 25*(5), 606-612. doi:10.1165/ajrcmb.25.5.4487

Chatterjee, S. (2011). Brain tuberculomas, tubercular meningitis, and post-tubercular hydrocephalus in children. *J Pediatr Neurosci, 6*(Suppl 1), S96-S100. doi:10.4103/1817-1745.85725

Christensen, A. S., Andersen, A. B., Thomsen, V. O., Andersen, P. H., & Johansen, I. S. (2011). Tuberculous meningitis in Denmark: a review of 50 cases. *BMC Infect Dis, 11*, 47. doi:10.1186/1471-2334-11-47

Dallenga, T., Linnemann, L., Paudyal, B., Repnik, U., Griffiths, G., & Schaible, U. E. (2018). Targeting neutrophils for host-directed therapy to treat tuberculosis. *Int J Med Microbiol, 308*(1), 142-147. doi:10.1016/j.ijmm.2017.10.001

Donald, P. R., & Schoeman, J. F. (2004). Tuberculous meningitis. *N Engl J Med, 351*(17), 1719-1720. doi:10.1056/NEJMp048227

Donald, P. R., & Schoeman, J. F. (2009). Central nervous system tuberculosis in children. In H. S. Schaaf, A. I. Zumla, J. M. Grange, M. C. Raviglione, W. W. Yew, & J. R. Stark (Eds.), *Tuberculosis* (pp. 413-423): W. B. Saunders.

Irwin, S. M., Driver, E., Lyon, E., Schrupp, C., Ryan, G., Gonzalez-Juarrero, M., . . . Lenaerts, A. J. (2015). Presence of multiple lesion types with vastly different microenvironments in C3HeB/FeJ mice following aerosol infection with Mycobacterium tuberculosis. *Dis Model Mech, 8*(6), 591-602. doi:10.1242/dmm.019570

Karstaedt, A. S., Valtchanova, S., Barriere, R., & Crewe-Brown, H. H. (1998). Tuberculous meningitis in South African urban adults. *QJM, 91*(11), 743-747. doi:10.1093/qjmed/91.11.743

Kramnik, I., Dietrich, W. F., Demant, P., & Bloom, B. R. (2000). Genetic control of resistance to experimental infection with virulent Mycobacterium tuberculosis. *Proc Natl Acad Sci U S A, 97*(15), 8560-8565. doi:10.1073/pnas.150227197

Lammie, G. A., Hewlett, R. H., Schoeman, J. F., & Donald, P. R. (2009). Tuberculous cerebrovascular disease: a review. *J Infect, 59*(3), 156-166. doi:10.1016/j.jinf.2009.07.012

Lee, S. C., Dickson, D. W., Liu, W., & Brosnan, C. F. (1993). Induction of nitric oxide synthase activity in human astrocytes by interleukin-1 beta and interferon-gamma. *J Neuroimmunol, 46*(1-2), 19-24. doi:10.1016/0165-5728(93)90229-r

Manca, C., Tsenova, L., Barry, C. E., 3rd, Bergtold, A., Freeman, S., Haslett, P. A., . . . Kaplan, G. (1999). Mycobacterium tuberculosis CDC1551 induces a more vigorous host response in vivo and in vitro, but is not more virulent than other clinical isolates. *J Immunol, 162*(11), 6740-6746.

Mazzolla, R., Puliti, M., Barluzzi, R., Neglia, R., Bistoni, F., Barbolini, G., & Blasi, E. (2002). Differential microbial clearance and immunoresponse of Balb/c (Nramp1 susceptible) and DBA2 (Nramp1

bioRxiv preprint doi: https://doi.org/10.1101/2021.08.15.456427; this version posted August 16, 2021. The copyright holder for this preprint (which was not certified by peer review) is the author/funder, who has granted bioRxiv a license to display the preprint in perpetuity. It is made available under aCC-BY-NC-ND 4.0 International license.

resistant) mice intracerebrally infected with Mycobacterium bovis BCG (BCG). *FEMS Immunol Med Microbiol, 32*(2), 149-158. doi:10.1111/j.1574-695X.2002.tb00547.x

Misra, U. K., Kalita, J., Srivastava, R., Nair, P. P., Mishra, M. K., & Basu, A. (2010). A study of cytokines in tuberculous meningitis: clinical and MRI correlation. *Neurosci Lett, 483*(1), 6-10. doi:10.1016/j.neulet.2010.07.029

Nagesh Babu, G., Kumar, A., Kalita, J., & Misra, U. K. (2008). Proinflammatory cytokine levels in the serum and cerebrospinal fluid of tuberculous meningitis patients. *Neurosci Lett, 436*(1), 48-51. doi:10.1016/j.neulet.2008.02.060

Olin, M. R., Armien, A. G., Cheeran, M. C., Rock, R. B., Molitor, T. W., & Peterson, P. K. (2008). Role of nitric oxide in defense of the central nervous system against Mycobacterium tuberculosis. *J Infect Dis, 198*(6), 886-889. doi:10.1086/591097

Ong, C. W., Pabisiak, P. J., Brilha, S., Singh, P., Roncaroli, F., Elkington, P. T., & Friedland, J. S. (2017). Complex regulation of neutrophil-derived MMP-9 secretion in central nervous system tuberculosis. *J Neuroinflammation, 14*(1), 31. doi:10.1186/s12974-017-0801-1

Peterson, P. K., Hu, S., Anderson, W. R., & Chao, C. C. (1994). Nitric oxide production and neurotoxicity mediated by activated microglia from human versus mouse brain. *J Infect Dis, 170*(2), 457-460. doi:10.1093/infdis/170.2.457

Porkert, M. T., Sotir, M., Parrott-Moore, P., & Blumberg, H. M. (1997). Tuberculous meningitis at a large inner-city medical center. *Am J Med Sci, 313*(6), 325-331. doi:10.1097/00000441-199706000-00002

Rock, R. B., Hu, S., Deshpande, A., Munir, S., May, B. J., Baker, C. A., . . . Kapur, V. (2005). Transcriptional response of human microglial cells to interferon-gamma. *Genes Immun, 6*(8), 712-719. doi:10.1038/sj.gene.6364246

Rock, R. B., Olin, M., Baker, C. A., Molitor, T. W., & Peterson, P. K. (2008). Central nervous system tuberculosis: pathogenesis and clinical aspects. *Clin Microbiol Rev, 21*(2), 243-261, table of contents. doi:10.1128/CMR.00042-07

Rom, W. N., Garay SM. (2004). *Tuberculosis* (2 ed.). Philadelphia: Lippincott Williams & Wilkins.

Saez-Llorens, X., Ramilo, O., Mustafa, M. M., Mertsola, J., & McCracken, G. H., Jr. (1990). Molecular pathophysiology of bacterial meningitis: current concepts and therapeutic implications. *J Pediatr, 116*(5), 671-684. doi:10.1016/s0022-3476(05)82647-2

Sanchez-Garibay, C., Hernandez-Campos, M. E., Tena-Suck, M. L., & Salinas-Lara, C. (2018). Experimental animal models of central nervous system tuberculosis: A historical review. *Tuberculosis (Edinb), 110*, 1-6. doi:10.1016/j.tube.2018.02.007

Schaller, M. A., Wicke, F., Foerch, C., & Weidauer, S. (2019). Central Nervous System Tuberculosis : Etiology, Clinical Manifestations and Neuroradiological Features. *Clin Neuroradiol, 29*(1), 3-18. doi:10.1007/s00062-018-0726-9

Schneemann, M., & Schoeden, G. (2007). Macrophage biology and immunology: man is not a mouse. *J Leukoc Biol, 81*(3), 579; discussion 580. doi:10.1189/jlb.1106702

Sharma, S., Goyal, M. K., Sharma, K., Modi, M., Sharma, M., Khandelwal, N., . . . Lal, V. (2017). Cytokines do play a role in pathogenesis of tuberculous meningitis: A prospective study from a tertiary care center in India. *J Neurol Sci, 379*, 131-136. doi:10.1016/j.jns.2017.06.001

Shaw, J. E. T., Pasipanodya, J. G., & Gumbo, T. (2010). Meningeal tuberculosis: high long-term mortality despite standard therapy. *Medicine (Baltimore), 89*(3), 189-195. doi:10.1097/MD.0b013e3181df9070

Shope, R. E., & Lewis, P. A. (1929). A Paralytic Disease of Guinea Pigs Due to the Tubercle Bacillus. *J Exp Med, 50*(3), 365-370. doi:10.1084/jem.50.3.365

Swaim, L. E., Connolly, L. E., Volkman, H. E., Humbert, O., Born, D. E., & Ramakrishnan, L. (2006). Mycobacterium marinum infection of adult zebrafish causes caseating granulomatous tuberculosis and is moderated by adaptive immunity. *Infect Immun, 74*(11), 6108-6117. doi:10.1128/IAI.00887-06

bioRxiv preprint doi: https://doi.org/10.1101/2021.08.15.456427; this version posted August 16, 2021. The copyright holder for this preprint (which was not certified by peer review) is the author/funder, who has granted bioRxiv a license to display the preprint in perpetuity. It is made available under aCC-BY-NC-ND 4.0 International license.

The Lancet, N. (2011). Tuberculosis of the CNS remains a lethal threat. *Lancet Neurol, 10*(5), 395. doi:10.1016/S1474-4422(11)70082-5

Tsenova, L., Mangaliso, B., Muller, G., Chen, Y., Freedman, V. H., Stirling, D., & Kaplan, G. (2002). Use of IMiD3, a thalidomide analog, as an adjunct to therapy for experimental tuberculous meningitis. *Antimicrob Agents Chemother, 46*(6), 1887-1895. doi:10.1128/aac.46.6.1887-1895.2002

Tsenova, L., Sokol, K., Freedman, V. H., & Kaplan, G. (1998). A combination of thalidomide plus antibiotics protects rabbits from mycobacterial meningitis-associated death. *J Infect Dis, 177*(6), 1563-1572. doi:10.1086/515327

Tucker, E. W., Pokkali, S., Zhang, Z., DeMarco, V. P., Klunk, M., Smith, E. S., . . . Kannan, S. (2016). Microglia activation in a pediatric rabbit model of tuberculous meningitis. *Dis Model Mech, 9*(12), 1497-1506. doi:10.1242/dmm.027326

van Well, G. T., Wieland, C. W., Florquin, S., Roord, J. J., van der Poll, T., & van Furth, A. M. (2007). A new murine model to study the pathogenesis of tuberculous meningitis. *J Infect Dis, 195*(5), 694-697. doi:10.1086/511273

Wilkinson, R. J., Rohlwink, U., Misra, U. K., van Crevel, R., Mai, N. T. H., Dooley, K. E., . . . Tuberculous Meningitis International Research, C. (2017). Tuberculous meningitis. *Nat Rev Neurol, 13*(10), 581-598. doi:10.1038/nrneurol.2017.120

Zaharie, S. D., Franken, D. J., van der Kuip, M., van Elsland, S., de Bakker, B. S., Hagoort, J., . . . Marceline van Furth, A. (2020). The immunological architecture of granulomatous inflammation in central nervous system tuberculosis. *Tuberculosis (Edinb), 125*, 102016. doi:10.1016/j.tube.2020.102016

Zucchi, F. C., Pelegrini-da-Silva, A., Neder, L., Silva, C. L., Tsanaclis, A. M., & Takayanagui, O. M. (2012). The contribution of a murine CNS-TB model for the understanding of the host-pathogen interactions in the formation of granulomas. *J Neurosci Methods, 206*(1), 88-93. doi:10.1016/j.jneumeth.2012.02.015